TUNING
THE EXCITON-PLASMON
COUPLING

A THESIS
SUBMITED TO THE DEPARTMENT OF PHYSICS
AND THE GRADUATE SCHOOL OF ENGINEERING AND SCIENCE
OF BILKENT UNIVERSTY
IN PARTIAL FULFILMENT OF THE REQUIREMENTS
FOR THE DEGREE OF
MASTER OF SCIENCE

By
Simge Ateş
August, 2012

I certified that I have read this thesis and that in my opinion it is fully adequate, in scope and quality, as a thesis for the degree of Master of Science.

_____
Prof. Dr. Atilla Aydınlı (Advisor)

I certified that I have read this thesis and that in my opinion it is fully adequate, in scope and quality, as a thesis for the degree of Master of Science.

_____
Assist. Prof. Dr. Coşkun Kocabaş

I certified that I have read this thesis and that in my opinion it is fully adequate, in scope and quality, as a thesis for the degree of Master of Science.

_____
Assist. Prof. Dr. Sinan Balcı

Approved for the Graduate School of Engineering and Science:

_____
Prof. Dr. Levent Onural
Director of the Graduate School

ABSTRACT
TUNING THE EXCITON-PLASMON COUPLING

Simge Ateş
M.S. in Physics
Supervisor: Prof. Dr. Atilla Aydınlı
August, 2012

Exciton-plasmon coupling has recently drawn much interest. In this work, FDTD simulations of exciton-plasmon coupling in plasmonic cavity structures with corrugation patterns are investigated. Excitonic modes are obtained from a Lorentz absorber modeling of a J-aggregate organic dye. The coupling of these excitonic and plasmonic modes on Ag thin films is demonstrated. Rabi splitting due to coupling was clearly observed. Flat metallic surfaces, uniform gratings and Moiré surfaces are used in simulations as corrugation patterns. Metal film thickness and dye concentration dependence of Rabi splitting via exciton-plasmon coupling was also observed on thin flat Ag films. We show that Rabi splitting occurs even at low dye concentrations, and the magnitude of splitting increases as dye concentration increases. A new state in the band gap is observed when the total oscillator strength is increased. Large Rabi splitting is observed when plasmon damping is modulated. Exciton-plasmon coupling on uniform gratings is studied as a function of cavity size, corrugation periodicity and depth. Q factor and Rabi splitting behavior of exciton-plasmon coupling on Moiré cavities are investigated as a function of cavity size. Strong anti-crossing is observed when the excitonic absorption matches with the cavity state.

Keywords: Exciton-Plasmon Coupling, Plasmonic Cavities, J-aggregates, Rabi Splitting

ÖZET
EKSİTON-PLAZMON ÇİFTLENMESİNİN AKORTLANMASI

Simge Ateş
Fizik, Yüksek Lisans
Tez Yöneticisi: Prof. Dr. Atilla Aydınlı
Ağustos, 2012

Eksiton-plazmon çiftlenmesi bu günlerde çok ilgi çekmektedir. Bu çalışmada, kıvrımlı plazmonik kovuk yapılarında eksiton-plazmon çiftlenmesi zamanda sonlu farklar yöntemi (FDTD) simulasyonlarıyla incelendi. Eksitonik kipler J-aggregate organik boyanın Lorentz soğurucu modellemesiyle elde edildi. Bu eksitonik ve plazmonik kiplerin Ag ince film üzerinde çiftlenmesi gösterildi. Çiftlenmeye bağlı Rabi yarılması açıkça gözlemlendi. Yassı metalik yüzeyler, tekdüze kırınım ağları ve Moiré yüzeyleri simulasyonlarda kıvrım desenleri olarak kullanıldı. Eksiton-plazmon çiftlenmesi yoluyla Rabi yarılmasının, metal film kalınlığı ve boya konsantrasyonu bağımlılığı da yassı ince Ag filmler üzerinde gözlemlendi. Düşük boya konsantrasyonunda Rabi yarılmasının oluştuğunu ve yarılma büyüklüğünün boya konsantrasyonu arttıkça arttığını gösterdik. Toplam osilatör kuvveti arttıkça, band aralığında yeni bir hal gözlemlendi. Geniş Rabi yarılması ayrıca plasmon sönümlenmesi ayarlandığında gözlemlenmiştir. Tekdüze kırınınm ağları üzerinde exciton-plasmon çiftlenmesi kovuk genişliği, kırımın perioodisite ve derinliğinin bir fonksiyonu olarak çalışıldıMoiré yüzeylerinde eksiton-plasmon çiftlenmesinin Q faktör ve Rabi yarılması davranışları kovuk boyutuna göre incelendi. Eksitonik emilme ve kovuk kipi eşlendiğinde kuvvetli antikros gözlemlendi.

Anahtar sözcükler: Eksiton-plazmon çiftlenmesi, Plasmonik Kovuklar, J-aggregates, Rabi Yarılması.

Acknowledgement

I would like to express my deepest gratitude to my academic advisor Prof. Atilla Aydınlı for his guidance, support and encouragement during this study. He is the external force in the “Law of Inertia”.

I would also like to present my gratitude to Assist.Prof.Dr. Coşkun Kocabaş and Assist. Prof. Dr. Sinan Balci for their judgments and critics as the Master Thesis committee.

I wish to express my special thanks to Ertuğrul Karademir for his enlightening mentorship and advices, and also his patience during my thesis flip outs.

I am indebted to my parents for their endless love, support and patience. I also would like to thank my sister Sezgi Ateş for seeing me as “wonder woman”.

I would like to thank the “last Amazon” Özge Akay for her invaluable friendship from the very first week of freshman year of ODTU.

I would like to thank my office mates Abdullah Muti, Melike Gümüş, Seval Sarıtaş and Sinan Gündoğdu for creating productive studying environment. Working with them made the thesis process less painful.

This work was granted by Turkish Scientific and Technical Research Council (TUBITAK), grant no: 110T589.

Contents

List of Figures

List of Tables

Chapter 1

Introduction

Excion-plasmon coupling is a light matter interaction that results in hybrid particles. In this thesis, exciton-plasmon coupling is investigated on plasmonic cavities. In order to understand this interaction, exitonic sources are placed on various plasmonic surfaces, and plasmonic cavities with plasmonic band gaps. In this chapter, brief information about these structures and exciton-plasmon coupling is given followed by an overview of the thesis.

1.1 Surface Plasmons

Surface plasmons can be described as collective oscillations of surface electrons of a conductor. When the surface of a conductor is illuminated with an incident light, light couples with surface plasmons and leads to a hybrid particle called the surface plasmon polariton (SPP). Although SPs have been known since 1957 (Ritchie) [1], their importance became pronounced at the beginning of 2000s with H.A Atwater suggested their use in sensors and electronics [2]. The term plasmonics is used to describe the wide range of structures supporting surface plasmons and their applications. Examples of such applications are abounding in the literature. Latest developments in light-matter interaction show that surface plasmon polaritons have great contribution to light emission when the emitter is very near the surface [3]. Possibility of high throughput and high-efficiency SPP coupling via super-wavelength slits is shown by theoretical and numerical studies [4]. In addition, design, fabrication and also characterization of the subwavelength waveguide

structures are based on surface plasmons [5] [6]. For further reference several reviews may be consulted [7] [8]. Optical and electronic properties of SPPs lead to use of different SPP supporting structures like waveguides, cavities and lenses. One important reason for investigation of SPP structures is the limitations in the confinement of light in matter. SPPs provide the ability to confine light to very small volumes beyond the diffraction limit. Due to diffraction, light cannot be focused less than half of its wavelength ($\lambda/2$) by dielectric lenses, where λ is the wavelength in the dielectric medium. But surface plasmon structures allow us to confine light less then $\lambda/2$ by coupling it into sub-wavelength surface modes [9].

Advances in nanofabrication and synthesis of metallic nanomaterials resulted in variety of plasmonic nanostructures with the ability to confine SPPs leading to applications in biosensors, nanolasers, light emitting diodes, solar cells, spectroscopy, microfluidics, nanooptics, etc.

1.2 Plasmonic structures

Confinement of SPPs requires engineering of metallic surfaces. Metallic nanoparticles, 1-D and 2-D metallic waveguides as well as periodic structures such as gratings can be used for confinement. Grating can be fabricated in many different ways, starting with uniform sinusoidal profiles and extending to biharmonic and chirped forms. 1-D ve 2-D cavites can be fabricated using both electron beam and interference lithography. Plasmonic structures are issued various experimental and theoretical studies not only by means of application but also plasmonic structures such as plasmonic waveguides, lenses, cavities [7]. Plasmonic waveguides are used to guide light in subwavelength regions. Slab waveguides are most common and basic ones that light can be confined to one dimension. Altering the index difference between the surrounding medium and the slab is enough for guiding [6]. Existence of plasmonic cavities based on uniform gratings is demonstrated experimentally [10]. Such plasmonic structures can be used in the construction of many new devices including plasmonic lasers.

1.3 Coupling of plasmons with two level systems

Design of plasmonic lasers requires not only a cavity but also a gain medium. Gain may be provided through materials such as quantum dots, nanowires, dyes, polymer and the like. Typically such materials can be represented as a two level system interacting with the plasmonic surface. During the last decade light-matter interactions received a lot of attention, since they can form a hybrid state due to coupling of optical mode to excitonic modes of quantum system [11]. Excitonic sources like R6G (rhodamin6G) [12] , J-aggregates [13] polymers and quantum dots [14] can be considered as two level systems. It is well known that interaction of such excitonic syatems with the plasmonic modes leads to a splitting of the resonance called Rabi splitting. When the rate of energy transfer is larger than the decay rate, strong coupling is observed. Establishing the conditions for strong coupling requires the increase in the oscillator strength of the excitonic system as well as decreasing plasmonic losses. Providing a cavity for feedback increases strong coupling as well. Such cavities can be constructed using various approaches interacting with organic and inorganic semiconductors [15] [16]. This problem has been studied both theoretically and experimentally by various authors [17].

1.4 Other applications of plasmons

Plasmons have considerably wide application area from sensors to lasers. For example SPPs' sensitivity to surface conditions makes them favorable for the use of bio- and chemo- sensors [18]. In addition, surface plasmons' high field intensities make them suitable for single molecule detection in surface enhanced Raman spectroscopy (SERS) [19]. Moreover, plasmonics provides plasmonic lasers that reduce the restriction both in optical mode size and physical device dimension [20]

1.5 Overview

In this thesis, exciton-plasmon coupling is studied on plasmonic surfaces as flat metal surfaces, uniform gratings and Moiré surfaces. A special aggregated dye

molecules in polymer matrix with strong and sharp absorption in the visible region of the electromagnetic spectrum, J –aggregate is used as the excitonic source.

In chapter 2, general information about surface plasmons and surface plasmon polaritons (SPPs) are given. Drude-Sommerfeldt model is derived to display plasmon characteristics. Localized plasmons and plasmonic cavity structures are studied to understand the types of plasmonic sources in exciton-plasmon coupling. A review of theoretical background of the exciton-plasmon coupling is explained. Conditions for exciton-plasmon strong coupling which are the reason of Rabi splitting are discussed.

In chapter 3 optical characterizations of cyanine dye molecules in polymer matrix thin films is explained in the experimental part of the work.

Optical properties of excitonic materials are critical in the coupling of the two level exciton systems with surface plasmons. Therefore, in chapter 3 optical characterizations of cyanine dye in polymer matrix thin films is explained and the results are discussed in detail.

In chapter 4 simulations of exciton-plasmon coupling on flat metal surfaces, uniform gratings and Moiré surfaces are given. In the first part of this chapter, brief information about Lumerical FDTD Solutions software package, is given since it is used for the numerical calculations of the relevant equations for exciton-plasmon coupling. Effects of Lorentz oscillator strength and metal thin film thickness on exciton-plasmon coupling on flat metal surfaces are studied. In order to understand exciton-plasmon coupling on uniform gratings, depth and periodicity of the gratings are varied in a controlled manner. Moreover, exciton-plasmon coupling in plasmonic cavity structures is studied by tuning the cavity size of Moiré surfaces.

In chapter 5, results and a comprehensive analysis of the simulations are summarized. Finally, future work and possible applications are discussed.

Chapter 2

Theoretical Background

In this part of the thesis, we summarize basic theoretical background of the exciton-plasmon coupling on plasmonic cavities. Initially, properties of the plasmons and surface plasmon polaritons will be discussed. Coupling techniques of light into plasmons are also described to lead us in exciton-plasmon coupling. To improve our understanding about exciton-plasmon coupling, brief description of Rabi oscillations and strong coupling regime are stated. Finally, numerical approach consisting of finite difference in the time domain is explained to provide the background for our results.

2.1 Plasmons

Plasmons are the quanta of collective oscillations of free or nearly free electrons. As such they are quasiparticles like phonons. They are mainly observed in metals. They can be observed both in the bulk as well as on the surface. Bulk plasmons are typically observed with electron energy loss spectroscopy with energies of up to 50 eV. Surface plasmons are longitudinal electromagnetic waves that are confined to the interfaces. Surface plasmons can also be thought of as the normal modes of charge fluctuation or charge density waves at a metallic surface. In this thesis we concentrate on surface plasmons. Metals have complex permittivity and behavior of plasma oscillations can be understood using the free electron model. We have defined plasmon as collective oscillation of conduction electrons. The coupling of this plasma oscillation with incident beam of photons creates surface plasmon polaritons (SPP). SPPs can propagate along the interface between a metal and a

dielectric medium. In order to investigate this propagation, Maxwell equations must be solved like in all classical electromagnetic phenomena. Maxwell equations for macroscopic electromagnetism are [21],

$$\nabla . \mathbf{D} = \rho_{ext} \tag{2.1}$$

$$\nabla \times \mathbf{H} = \boldsymbol{J}_{ext} + \frac{\partial \mathbf{D}}{\partial t} \tag{2.2}$$

$$\nabla . \mathbf{B} = 0 \tag{2.3}$$

$$\nabla \times \mathbf{E} + \frac{\partial \mathbf{B}}{\partial t} = 0 \tag{2.4}$$

where D is dielectric displacement, E is the electric field, B is the magnetic inductance and H is the magnetic field. $\boldsymbol{J}_{ext}$ and ρ_{ext} are external current and charge density, respectively. Maxwell equations should be applied on the semi-infinite and flat interface between conductor and dielectric to understand behavior of SPPs.

Writing in terms of total current and charge, Maxwell equations can be related to each other by means of the polarization **P** and magnetization **M** by

$$\mathbf{D} = \epsilon_0 \mathbf{E} + \mathbf{P} \tag{2.5}$$

$$\mathbf{H} = \frac{1}{\mu_0} \mathbf{B} - \mathbf{M} \tag{2.6}$$

where ϵ_0 is electric permittivity and μ_0 is magnetic permeability of vacuum. In case of isotropic and linear media, equations (2.5) and (2.6) could be restated as

$$\mathbf{D} = \epsilon_0 (1 - x_e) \mathbf{E} = \epsilon \mathbf{E} \tag{2.7}$$

$$\mathbf{B} = \mu_0 (1 - x_m) \mathbf{E} = \mu \mathbf{H} \tag{2.8}$$

where ϵ and μ are permittivity and permeability of the medium respectively. In addition x_e and x_m are electric and magnetic susceptibility of the medium where $\mathbf{P} = \epsilon_0 x_e \mathbf{E}$ and $\mathbf{M} = x_m \mathbf{H}$. Finally, Maxwell equations take the form of

$$\boldsymbol{\nabla}.\mathbf{E} = \frac{\rho_{ext}}{\epsilon} \tag{2.9}$$

$$\boldsymbol{\nabla}.\mathbf{B} = 0 \tag{2.10}$$

$$\boldsymbol{\nabla} \times \mathbf{E} = -\frac{\partial \mathbf{B}}{\partial t} \tag{2.11}$$

$$\boldsymbol{\nabla} \times \mathbf{B} = \mu \boldsymbol{J}_{ext} + \mu\epsilon \frac{\partial \mathbf{E}}{\partial t} \tag{2.12}$$

In the absence of external current and charge, by taking curl of equation 2.10 and then inserting equation (2.11) into it, one can obtain

$$\nabla \times \nabla \times \mathbf{E} = -\mu_0 \frac{\partial^2 \mathbf{D}}{\partial t^2} \tag{2.13}$$

By using vector identity $\nabla \times \nabla \times \mathbf{E} = \nabla(\nabla.\mathbf{E}) - \nabla^2\mathbf{E}$ and being aware of $\boldsymbol{\nabla}.\mathbf{E} = 0$, in this case, one can form an electromagnetic wave equation

$$\boldsymbol{\nabla^2}.\mathbf{E} = \mu\sigma \frac{\partial \mathbf{E}}{\partial t} + \mu\epsilon \frac{\partial^2 \mathbf{E}}{\partial t^2} \tag{2.14}$$

where σ is the conductivity of the metal which come from the ohms law $\mathbf{J}_{\boldsymbol{ext}} = \sigma\mathbf{E}$. Assuming a harmonic form for E-field $\mathbf{E}(t) = \mathbf{E}(\mathbf{r})e^{-i\omega t}$ and inserting $\mathbf{E}(t)$ into 2.21, Helmholtz wave equation can be obtained.

$$\boldsymbol{\nabla^2}.\mathbf{E} + \boldsymbol{\omega^2}\mu\epsilon\mathbf{E}(\mathbf{r}) = 0 \tag{2.15}$$

where $\in$ is known as so-called complex permittivity in the form of

$$\epsilon = \epsilon + \frac{i\sigma}{\omega} \tag{2.16}$$

Here σ conductivity is also complex and to understand this complex behavior one should be aware of Drude –Sommerfeld model. Valence electrons in a metal behave like a gas of free electrons and oscillate with respect to immobile ion cores. Electron-electron and electron-ion interactions that occur because of collisions are ignored and collisions are assumed instantaneous in the Drude-Sommerfeld model. It describes the response of the electrons to an external driving field revealing information on the optical properties of metals.

Ignoring the magnetic field, B, we start by considering an external incident light on a metallic surface. The spatial variation of the field is also ignored. This is acceptable unless the field varies much over distances comparable with the electrons mean free path. In the Drude model, equation of the motion for an electron is [22],

$$m^* \frac{d\mathbf{v}(t)}{dt} = -\frac{m^*}{\tau}\,\mathbf{v}(t) - e\mathbf{E}(t) \tag{2.17}$$

where e and m^* are charge and effective mass of the electrons in a crystal respectively and τ is the relaxation time. Assuming the driving E-field has harmonic time dependence, $\mathbf{E}(t) = \mathbf{E_0}e^{-i\omega t}$, and substituting $\mathbf{E}(t)$ into equation (2.17) gives mean velocity as,

$$\mathbf{v}(t) = -\frac{e\tau}{m^*(1 - i\omega\tau)}\mathbf{E}(t) \tag{2.18}$$

which is in the form of $\mathbf{v}(t) = \mathbf{v_0}e^{-i\omega t}$. By substituting $\mathbf{v}(t)$ into the current density equation, $\mathbf{J_{ext}} = -ne\mathbf{v}$, one can get

$$\mathbf{J_{ext}} = \frac{ne^2\tau}{m^*(1 - i\omega\tau)}\mathbf{E}(t) \tag{2.19}$$

where n is the number of conduction electrons per unit volume. Comparing equation (2.19) with ohms law $\mathbf{J}_{ext} = \sigma \mathbf{E}$, conductivity is obtained as

$$\sigma = \frac{ne^2\tau}{m^*(1 - i\omega\tau)} \tag{2.20}$$

By using complex permittivity equation $\epsilon = \epsilon + \frac{i\sigma}{\omega}$ which will be obtained from Helmholtz wave equations in part 2.18, an expression for the complex permittivity can be derived as

$$\epsilon = \epsilon - \frac{\omega_p^2 \epsilon_0}{\omega^2 + i\omega/\tau} \tag{2.21}$$

where ω_p is defined as the plasma frequency;

$$\omega_p^2 = \frac{ne^2}{\epsilon_0 m^*} \tag{2.22}$$

In equation (2.21) first term is result of the bound charges in metal and the second one is due to the free electrons. By dividing both sides of the equation, the relative complex permittivity ($\epsilon_r = \epsilon / \epsilon_0$) takes the form of

$$\epsilon_r = 1 - \frac{\omega_p^2}{\omega^2 + i\omega/\tau} \tag{2.23}$$

To get a better understanding, we separate equation 2.23 into its real and imaginary parts in the form of $\epsilon_r = \epsilon_r' + i\epsilon_r''$, that gives the results,

$$\epsilon_r' = 1 - \frac{\omega_p^2 \tau^2}{1 + \omega^2\tau^2} \tag{2.24}$$

$$\epsilon_r'' = \frac{\omega_p^2 \tau^2}{\omega(1+\omega^2\tau^2)} \tag{2.25}$$

For the wavelengths that are visible or shorter $\omega\tau \gg 1$ and $\tau \approx 10^{-15}s$ at room temperature [22], so ϵ_r' (real part) can be estimated as

$$\epsilon_r' \approx 1 - \frac{\omega_p^2}{\omega^2} \tag{2.26}$$

For $\omega < \omega_p$ equation (2.26) becomes negative. Negative real relative permittivity makes metals highly reflective. On the other hand $\omega > \omega_p$ condition makes ϵ_r' positive and Helmholtz wave equation (2.15) give oscillatory solutions and the metal becomes transparent. Therefore, it can be concluded that plasma frequency is the frequency that metal starts to be transparent against the incoming light. The coupling of plasma to the incoming light is the simplest explanation of the formation of SPPs. The major condition in this coupling event is the resonance with plasma frequency.

Interband transitions and real metals

The Drude-Sommerfeld model gives quite precise results for the optical properties of metals in the infrared regime. However it needs to be extended in the visible range by considering the response of bound electrons as well. As an example, for gold, at wavelengths those are shorter than ~ 550 nm, imaginary part of the measured dielectric function increases much more strongly as stated by the Drude-Sommerfeld theory [23]. The reason is that electrons of lower-lying bands can be promoted into the conduction band by higher energy photons. Excitation of the oscillation of bound electrons may describe such transitions, in a classical picture. The equation of motion for a bound electron reads as

$$m\ddot{\boldsymbol{x}} + m\gamma\dot{\boldsymbol{x}} + m\omega_0^2\boldsymbol{x} = -e\mathbf{E} \tag{2.27}$$

where m is the effective mass of the bound electron, which is in general different from the effective mass of a free electron in a periodic potential, γ is the damping

constant, and ω_0 bound electron resonance frequency. Solving the equation 2.27 to model $\epsilon_r(\omega)$ for noble metals lead us to a term in the form of

$$\epsilon_r(\omega) = 1 + \frac{\omega_p^2}{\omega_0^2 - \omega^2 - i\gamma\omega} \tag{2.28}$$

called the Lorentz oscillator term due to its resonant nature besides the free electron result in the equation 2.23 [23]. Equation 2.28 can be rewritten by separating it into real and imaginary parts as $\epsilon_r = \epsilon_r' + i\epsilon_r''$ where

$$\epsilon_r' = 1 + \frac{(\omega_0^2 - \omega^2)\omega_p^2}{(\omega_0^2 - \omega^2)^2 + \gamma^2\omega^2} \tag{2.29}$$

and

$$\epsilon_r'' = \frac{\gamma\omega\omega_p^2}{(\omega_0^2 - \omega^2)^2 + \gamma^2\omega^2} \tag{2.30}$$

While real part of the equation shows dispersion-like behavior, imaginary part shows resonant behavior.

2.1.1 Dispersion Relation

In order to understand the relation between the plasma frequency and its wavevector, we start with Maxwell equations and obtain Helmholtz wave equations. Solving these equations under appropriate boundary conditions leads us to the dispersion relation. Helmholtz wave equation in the absence of external charge and current is

$$\boldsymbol{\nabla^2}.\mathbf{E} + k_0^2\epsilon\mathbf{E}(\mathbf{r}) = 0 \tag{2.31}$$

where $k_0 = \frac{\omega}{c}$ is the propagating wave vector.

We assume a linear interface of two homogenous, non-magnetic ($\mu = 1$) and optically isotropic medium and with the upper material as the dielectric with dielectric constant ϵ_1 and a metal with frequency dependent complex permittivity, $\epsilon_2(\omega) = \epsilon'(\omega) + \mathrm{i}\epsilon''(\omega)$, for other half of the space.

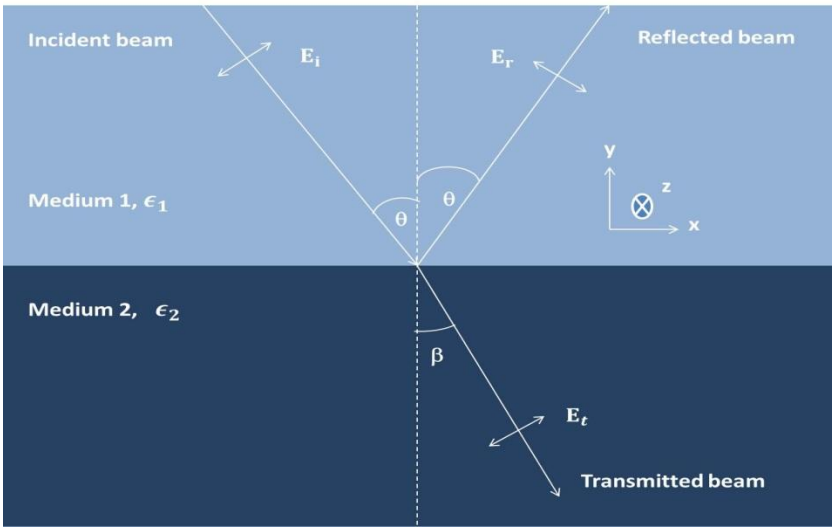

Figure 2.1 Planar interface geometry. Z-direction is into the page and propagation is in x-direction. Incident radiation is p-polarized ($\boldsymbol{\epsilon_2 > \epsilon_1}$).

For the interface geometry, which is shown in Figure 2.1, propagating waves can be described as $\mathbf{E}(x, y, z) = \mathbf{E}(y)e^{i\beta x}$ where β is the wave vector in the direction of propagation and called propagation constant ($\beta = k_x$). By inserting this expression into equation (2.31), gives

$$\frac{\partial^2 \mathbf{E}(z)}{\partial y^2} + (k_0^2 \epsilon - \beta^2)\mathbf{E} \tag{2.32}$$

From the equation (2.18),

$$\frac{\partial E_z}{\partial y} - \frac{\partial E_y}{\partial z} = i\omega\mu_0 H_x \tag{2.33}$$

$$\frac{\partial E_x}{\partial z} - \frac{\partial E_z}{\partial x} = i\omega\mu_0 H_y$$

$$\frac{\partial E_y}{\partial x} - \frac{\partial E_x}{\partial y} = i\omega\mu_0 H_z$$

From the equation (2.19),

$$\frac{\partial H_z}{\partial y} - \frac{\partial H_y}{\partial z} = i\omega\mu_0 E_x \tag{2.34}$$

$$\frac{\partial H_x}{\partial z} - \frac{\partial H_z}{\partial x} = i\omega\mu_0 E_y$$

$$\frac{\partial H_y}{\partial x} - \frac{\partial H_x}{\partial y} = i\omega\mu_0 E_z$$

Due to propagation in x-direction ($\frac{\partial}{\partial x} = i\beta$) and homogeneity in z-direction which means $\frac{\partial}{\partial z} = 0$, equations (2.33) and (2.34) can be simplified to below set of equations.

$$\frac{\partial E_z}{\partial y} = i\omega\mu_0 H_x \; and \; \frac{\partial H_z}{\partial y} = i\omega\mu_0 E_x \tag{2.35}$$

$$i\beta E_z = -i\omega\mu_0 H_y \; and \; H_z = -i\omega\mu_0 E_y$$

$$i\beta E_y - \frac{\partial E_x}{\partial y} = i\omega\mu_0 H_z \; and \; i\beta H_y - \frac{\partial H_x}{\partial y} = i\omega\mu_0 E_z$$

Above equations can be solved for both s and p polarized modes for propagating waves. In SPP wave only TM modes are allowed, we can continue with only p-polarized equations which means that E_x, E_y and H_z components exist. That leads us to analogous set of

$$E_x = \frac{1}{\omega\epsilon_0\epsilon}\frac{\partial H_z}{\partial y} \; and \; E_z = -\frac{1}{\omega\epsilon_0\epsilon} H_y \tag{2.36}$$

and TM mode wave equation takes the form of,

$$\frac{\partial^2 H_z}{\partial y^2} + (k_0^2\epsilon - \beta^2)H_z = 0 \tag{2.37}$$

After obtaining general sets of equations for TM modes, one can solve them for both upper and lower part of the Figure 2.1.

TM solutions to equation set of (2.36) and (2.37) for y<0 are

$$H_z(y) = A_1 e^{ik_1 y} e^{i\beta x} \tag{2.38}$$

$$E_x(y) = \frac{-iA_1 k_1}{\omega \epsilon_0 \epsilon_1} e^{ik_1 y} e^{i\beta x}$$

$$E_y(y) = \frac{-A_1 \beta}{\omega \epsilon_0 \epsilon_1} e^{ik_1 y} e^{i\beta x}$$

and for y>0 are

$$H_z(y) = A_2 e^{-k_2 y} e^{i\beta x} \tag{2.39}$$

$$E_x(y) = \frac{iA_2 k_2}{\omega \epsilon_0 \epsilon_2} e^{-k_2 y} e^{i\beta x}$$

$$E_y(y) = \frac{-A_1 \beta}{\omega \epsilon_0 \epsilon_2} e^{-k_2 y} e^{i\beta x}$$

k_1 and k_2 are perpendicular component of the wave vector in the y-direction at the interface of both media. The boundary conditions and the continuity at the interface yields equations (2.38) and (2.39) to $A_1 = A_2$ and

$$\frac{k_2}{k_1} = -\frac{\epsilon_2}{\epsilon_1} \tag{2.40}$$

and

$$k_1^2 = \beta^2 - k_0^2 \epsilon_1 \tag{2.41}$$

$$k_2^2 = \beta^2 - k_0^2 \epsilon_2$$

Combining equation (2.40) and (2.41) gives SPP condition.

$$\beta = k_x = k_0 \sqrt{\frac{\epsilon_1 \epsilon_2}{\epsilon_1 + \epsilon_2}} \tag{2.42}$$

For Drude model in vacuum ($\epsilon_2 = 1$) equation 2.42 gives

$$k_x = \frac{\omega}{c} \sqrt{\frac{\omega^2 - \omega_p^2}{2\omega^2 - \omega_p^2}} \tag{2.43}$$

To obtain the dispersion relation for surface plasmons, we take ω out of the equation 2.43;

$$\omega^2(k_x) = \frac{\omega_p^2}{2} + c^2 k_x^2 - \sqrt{\frac{\omega_p^4}{4} + c^4 k_x^4} \tag{2.44}$$

After normalizing equation 2.44 with respect to ω_p, one can plot dispersion behavior of SPPs,

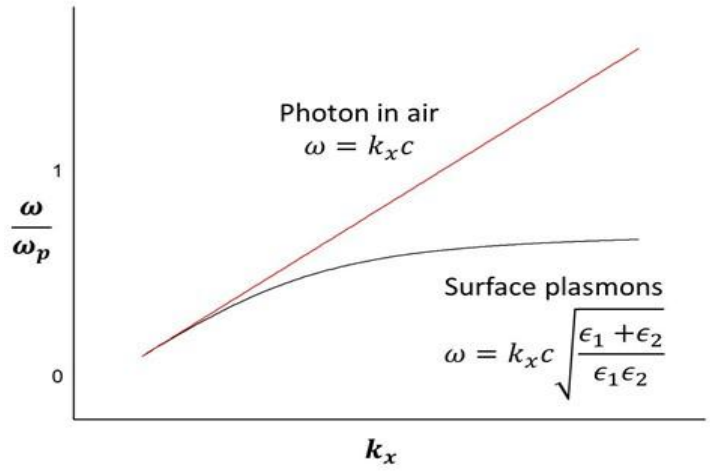

Figure 2.2 Dispersion Relation of SPP

As we can see clearly in Figure 2.2 there is a momentum mismatch between the incident light and SPs. Coupling of light in to the plasmonic modes is only possible by overcoming this mismatch.

Skin depth

The electromagnetic field associated with the SPPs decays evanescently in the direction perpendicular to the interface (y-direction) which is shown in Figure 2.3

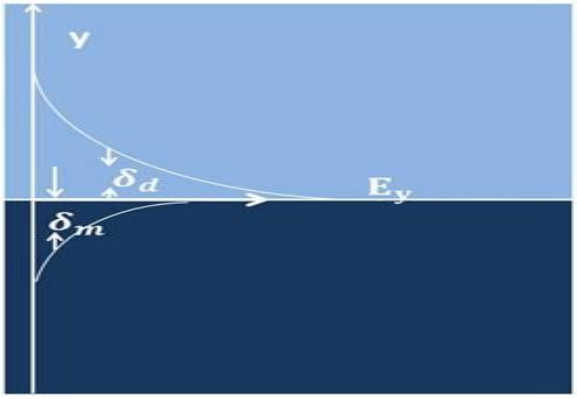

Figure 2.3 SPP on metal dielectric interface. Electromagnetic field intensity decays with the distance away from the surface.

When the surface-plasmon condition of equation (2.42) introduced into equation (2.41), the following expression for the surface-plasmon decay constant k_i, which is perpendicular to the interface can be found:

$$k_i = \frac{\omega}{c}\sqrt{\frac{\epsilon_i^2}{\epsilon_1 + \epsilon_2}} \tag{2.45}$$

where i=1,2 in y-direction. The evanescent field in Figure 2.3 is the result of quantum confinement due to $1/|k_y|$. When one side of the interface is assumed to be vacuum, the attenuation length is larger than the wavelength involved ($1/l_i > 1/k_y$), that is at long wavelength ($k_y \rightarrow 0$), the attenuation length into the metal is determined by the so-called skin depth. At large k_y the skin depth is $\delta_i \sim 1/k_y$ which implies a strong concentration of the surface-plasmon field near the interface.

2.2.2 Excitation of SPPs

Optical coupling of the incident light to surface plasmon modes, means that incident light and SPs are in resonance. In order to reach this resonance condition, momentum mismatch between the incident light and SPs must be overcome by momentum enhancement of the incident light. There are various ways to overcome this momentum mismatch such as prism coupling, grating coupling, near field coupling and diffraction from a surface defect. We will focus mainly on prism coupling as well as grating coupling since they are most commonly used to overcome momentum mismatch.

The simplest configuration to explain is diffraction from a surface defect (Figure 2. 4.a), since there is no specific way to satisfy SPP excitation conditions (reflection in almost every direction). SPP excitation can be achieved randomly because the diffracted component of the beam will have all wave vectors in near-field region. Although, it is the simplest one, this method has a major disadvantage which is its low coupling efficiency [8].

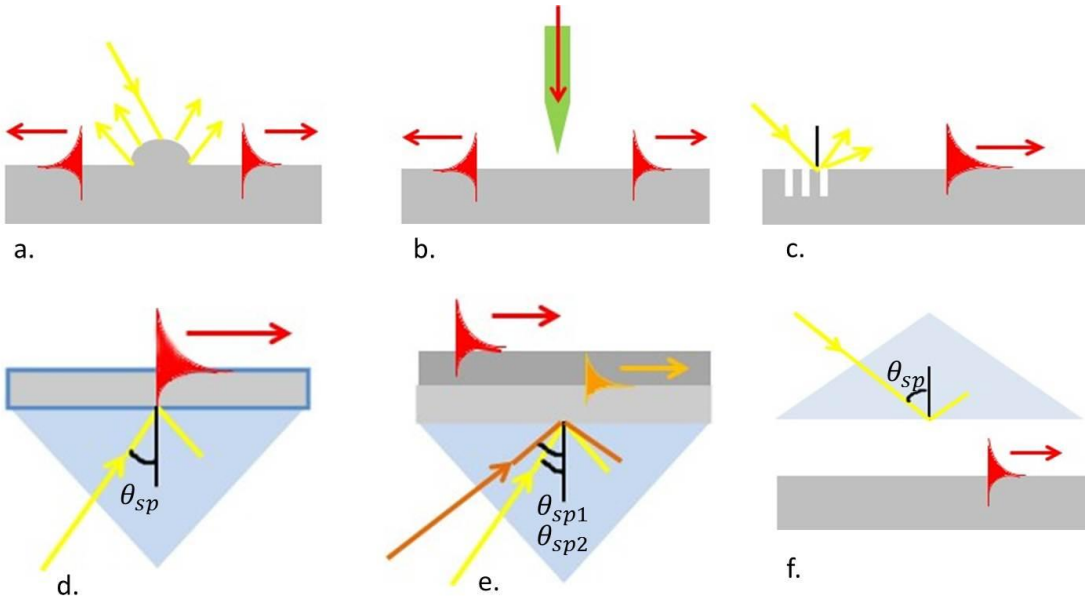

Figure 2. 4 SPP coupling configurations. a. is diffraction on a surface defect, b. is Near-Field coupling, c. is grating coupler, and prism Coupling's three main types shown d. Kretschmann configuration, e. two layer Kretschman configuration, (f) Otto configuration.

Near-field coupling technique is performed by scanning near-field optical microscopy (SNOM). Due to the illumination through SNOM fiber tip, SPPs can be excited locally on the surface [8]. This excitation process can be the result of diffraction (as in STM) or tunneling (as in AFM) of SPPs.

Grating coupling configuration is based on diffraction from periodically corrugated surface. First observation of excitation of SPPs by using grating coupling was made by Woods in. The simple way to think of the grating coupling is simple sinusoidal shape for the grating that can be defined by a grating vector

$$|\boldsymbol{G}| = \frac{2\pi}{\Lambda} \tag{2.46}$$

where Λ is grating period. When grating groves act like arrays of scattering centers, constructive interference of scattered waves generate a field in different diffraction orders. For a given order, if the wave vectors of the in-plane component matches the plasmonic dispersion relation (2.42), plasmons are excited.

Prism coupling is another optical excitation technique of SPPs. There are two known prism coupling configurations Otto (Figure 2.4.f) and Kretschman (Figure 2.4.d-e). A high index prism is employed to enhance the momentum of the incoming radiation by using the total internal reflection phenomena. Coupling takes place for the incidence angle that is larger than prism's critical angle. Both configurations requires same SPP coupling condition, which is

$$k_{sp} = \frac{\omega}{c}\sqrt{\epsilon_{prism}}\sin\theta \tag{2.47}$$

However, propagation interface shows differences for Otto and Kretschman configurations. In Otto configuration, metal under the prism is optically infinite and there is a gap between prism and metal. SPPs move along metal surface on the side of the gap. Coupling efficiency depends on the thickness of the gap. In Kretschmann configuration, there is no gap between prism and metal. Metal is directly on the

prism and there is a low index dielectric material, which can be air as in the case of Figure 2.4.d, on the metal. SPPs move along metal dielectric interface and metal. Metal thickness is crucially important for high coupling efficiency. Excessively thick metal layer prevents E-field to cross over metal. If metal is too thin, field passes through the metal easily and propagates freely [7].

2.3 Localized SPPs

So far we have described SPPs only on planar metal dielectric interfaces. These SPPs are propagating SPPs. However, metal dielectric interface of arbitrary geometries shows similar characteristics with the SPPs on planar interface except that they are localized. Localized plasmons occur at the characteristic frequency of the surface plasmons [7]. The first observation of localized plasmon is in the fourth century on a famous-Roman goblet. This goblet is made up of a glass in which gold and silver nanoparticles are located. The goblet is seen as green in reflection and red in transmission [2]. Optical properties of these particles can be widely tuned by altering their shape, size and composition. Localization of SPPs has wide application area from surface enhanced Raman spectroscopy to sensing and medical diagnostic applications [24]. Besides metal nanoparticles, uniform gratings, biharmonic gratings and Moiré surfaces can be used to form cavity structures which localize plasmons [10]. Moreover, omnidirectional localization of SPPs on the 2D Moiré surface has also been studied and is promising for lasing applications [25].

2.3.1 Plasmonic Cavities

Plasmonic cavities can be used to localize propagating plasmons, but they all show different characteristics due to their design difference and confinement mechanism. In this thesis, especially two types of periodic structures are emphasized. These are uniform gratings and Moiré surfaces.

Uniform Gratings are plasmonic band gap cavities with a period generally in the form of a sine function. Interaction of SPPs with the grooves which act as scattering centers, makes them backscattered which resulted with the formation of SPP standing waves. Two standing waves with different energies are formed due to

symmetry. Two modes are introduced; one is localized at the valleys while the other is localized over the grooves (Figure 2.5.b). When the wavelengths which corresponds to these energies (ω_+ and ω_-) destructively interfere there occur a band gap since waves cannot propagate in this region. (Figure 2.5.a). In addition group velocity of plasmons goes to zero at the band edges [10].

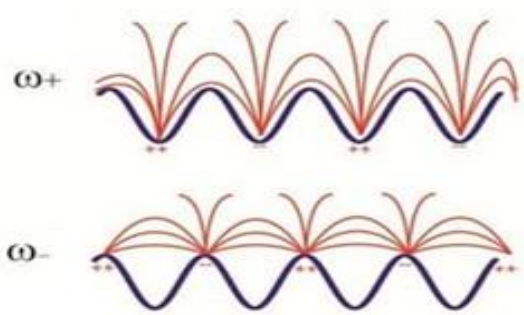

Figure 2.5 Uniform grating band structure.

ω_+ and ω_- modes have different confinement properties. That means we can tune width and position of the band gap by altering thickness of the dielectric layer [10].

Moiré Surfaces are obtained by supperimposing two sine functions with slightly different periods (Λ_1 and Λ_2). As such surface profile can be express with the formula,

$$S(x) = \cos(Gx)\sin(gx) \tag{2.48}$$

where

$$g = \frac{2\pi}{d} = 2\pi\frac{\Lambda_1 + \Lambda_2}{2\Lambda_1\Lambda_2} \tag{2.49}$$

and

$$G = \frac{2\pi}{D} = 2\pi\frac{\Lambda_1 - \Lambda_2}{2\Lambda_1\Lambda_2} \tag{2.50}$$

d is uniform periodicity and D is the periodicity of superstructure which defines the cavity size (see Figure 2.7).

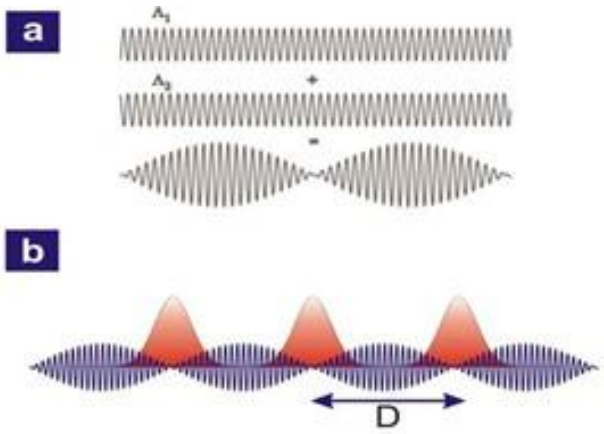

Figure 2.6 Moiré formation [26].

Since surface profile function is an odd function, structure is not symmetric at the nodes [27].

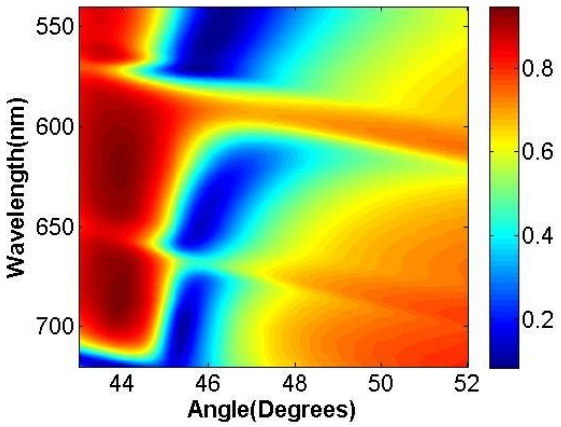

Figure 2.7 Typical dispersion spectrum of Moiré surfaces

Unlike the uniform gratings, there occur two band gaps and a cavity state where surface plasmons are confined.

2.4 Exciton-Plasmon Coupling

Exciton-plasmon coupling is a light matter interaction. There are tree important parameter in defining strong coupling, which is listed in Table 1

g	The rate at which the light and matter transfer energy
κ	The rate at which light escapes the cavity
γ	The rate at which matter loses its polarization

Table 1 Strong coupling parameters

Strong coupling of light and matter occurs when the ligth and matter energy transfer rate g is much higher than κ and γ. Periodical energy exchange occurs between light and matter in this limit [28]. At rate g when a microcavity and matter frequencies resonance, transmittance and reflectance spectrum indicates two new resonance frequencies.

$\omega_{cavity} = \omega_{exciton} = \omega_0$ → new frequency $\omega_{\mp} = \omega_0 \mp$ g

Due to this strong coupling, Rabi splitting occurs. To understand Rabi splitting, Rabi oscillations should be studied first.

2.4.1 Rabi Oscillations /Semi-classical Approach

Rabi oscillations are periodical transitions, which take place between stationary states of two-state quantum systems near an oscillatory driving field. The field can be expressed as

$$\mathbf{E}(\mathrm{t}) = \mathrm{E}_{\mathbf{0}} \cos(\omega t) \tag{2.51}$$

with frequency close to resonance $|\omega - \omega_0| \ll \omega_0$.

The atom-field interaction is described by the interaction Hamiltonian and the interaction Hamiltonian can be seen as the energy flow between the atom and the field

$$\widehat{H}^I(t) = \hat{\mathbf{d}} \cdot \mathrm{E}(t) = -\hat{d} \cos(\omega t) \tag{2.52}$$

where $\hat{\mathbf{d}}$ is the dipole moment operator. The total Hamiltonian of a quantum mechanical atom-field interacting system is

$$\hat{H} = \hat{H}_{atom} + \hat{H}_{field} + \hat{H}^I(t) \tag{2.53}$$

where $\hat{H}_{atom}$ is the free-atom Hamiltonian,

$$\hat{H}_{atom} = \frac{1}{2}\hbar\omega_{eg}(|e\rangle\langle e| - |g\rangle\langle g|) \tag{2.54}$$

Since there is no quantum field, total Hamiltonian becomes

$$\hat{H} = \hat{H}_{atom} + \hat{H}^I(t) = \hbar\omega_{eg}|e\rangle\langle e| - \hat{d}\cos(\omega t) \tag{2.55}$$

The state vector of the system is

$$|\Psi(t)\rangle = \sum_k C_k(t)e^{\frac{-iE_k t}{\hbar}}|k\rangle$$

$$= C_g(t)|g\rangle + C_e(t)e^{-i\omega_{eg}t}|e\rangle \tag{2.56}$$

Substituting this expansion in the time-dependent Schrödinger equation

$$i\hbar\frac{\partial|\Psi(t)\rangle}{\partial t} = \hat{H}|\Psi(t)\rangle \tag{2.57}$$

leads to the set of coupled first-order differential equations for the amplitudes

$$\dot{C}_g = -\frac{i}{h}E_0\cos(\omega t)\, d_{eg}e^{i\omega_{eg}t}C_e$$

$$\dot{C}_e = -\frac{i}{h}E_0\cos(\omega t)\, d^*_{eg}e^{-i\omega_{eg}t}C_g \tag{2.58}$$

After expanding $\cos(\omega t)$ and, applying the Rotating Wave Approximation (RWA) that means neglecting the quickly rotating terms since the time-evolution induced by the applied field is much slower than ω_0 one obtains

$$\dot{C}_g = 0$$

$$\dot{C}_e = -\frac{i}{2\hbar} E_0 d_{eg}^* e^{-i(\omega_{eg}-\omega)t} C_g \tag{2.59}$$

By integrating the differential equation (2.52) and introducing the detuning Δ (Δ= $\omega_{eg} - \omega$),

$$C_e = -\frac{i d_{eg}^* E_0}{\hbar} e^{\frac{i\Delta t}{2}} \sin\left(\frac{\Omega_R t}{2}\right) \tag{2.60}$$

Can be obtained [29] where

$$\Omega_R = \sqrt{\Delta^2 + \frac{\left(i d_{eg}^* E_0\right)^2}{\hbar^2}} \tag{2.61}$$

is the Rabi frequency. Δ in equation 2.60 is interaction energy between the plasmon and exciton which is also called Rabi splitting energy.

2.4.2 Rabi Splitting

The strong exciton-plasmon coupling leads to the formation of polaritonic states consisting of low- and high-energy polaritonic branches. Using coupled oscillator model and ignoring the damping effect, the energies of the polaritonic branches of the coupled oscillator system can be defined as

$$E_{1,2}(k) = \frac{1}{2}\left[E_{spp}(k) + E_{ex}\right] \mp \frac{1}{2}\sqrt{(\hbar\Omega_R)^2 + \left(E_{spp}(k) - E_{ex}\right)^2} \tag{2.62}$$

where k is the in plane wave vector, and E_1 and E_2 are the energies of the upper and lower polaritonic states, E_{ex} is the energy of the exciton, E_{spp} is the non-interacting plasmon energy, $\hbar\Omega_R$ is the Rabi splitting energy ($\hbar\Omega_R = 2V_0$ in which V_0 is the exciton-plasmon interaction energy occurring at the momentum at which energy

splitting between the polaritonic states reaches a minimum) occurring at the momentum value at which energy splitting between the polaritonic states reaches to a minimum value for a given momentum [28]. The Rabi coupling frequency increases with the strength of the exciton-plasmon interaction.

2.5 Simulation of exciton-plasmon

Plasmons are electromagnetic waves and excitons can be defined as particles with complex index of refraction. So their interaction can explained within electromagnetic theory. In other words, this interaction can be modeled by methods based on electromagnetic theory equations which can be solved with methods like FDTD method or transfer matrix method. In this thesis, we used FDTD method to solve Maxwell's equations for interacting excitons and plasmons.

2.5.1 FDTD method

Finite difference time domain method (FDTD) is an algorithm that provides easy way to solve Maxwell equations in complex geometries. FDTD method is a central difference method and gives information about both time and frequency.

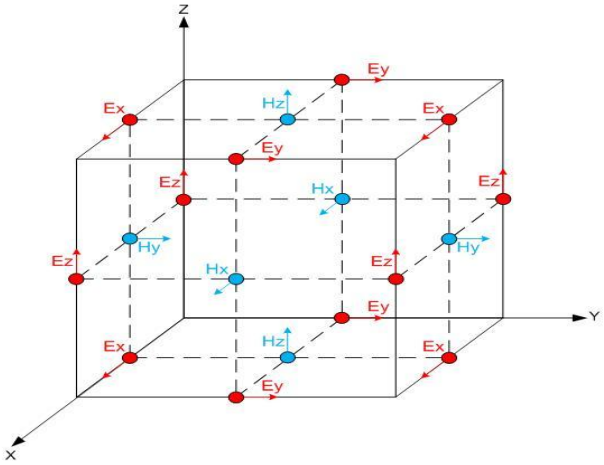

Figure 2.8 Cartesian Yee Cell, Electric and magnetic field vector components are placed on each other midway.

It is entirely vectorial method and solves Maxwell equations by meshing configurations in the so called Yee Cells (Figure 2.7). Maxwell equations are solved in these cells, then by integrating the solution for each cell each other desired

configurations is completed. Time is also discrete it is quantized into steps which are the time takes field to travel one cell to another.

For simplification one can start with Maxwell equations with no external charge and current,

Assuming linearity and ignoring frequency dependence of dielectric constant and focusing on transparent materials we can set as $\mathbf{D}(\mathbf{r}) = \epsilon_0\epsilon(\mathbf{r})\mathbf{E}(\mathbf{r})$ and $\mathbf{B}(\mathbf{r}) = \mu_0\mu(\mathbf{r})\mathbf{H}(\mathbf{r})$. For many dielectric materials $\mu(\mathbf{r})$ approaches unity so $\mathbf{B}(\mathbf{r}) = \mu_0\mathbf{H}(\mathbf{r})$. Under all these assumptions Maxwell equations transform into

$$\begin{gathered} \boldsymbol{\nabla}.[\epsilon(\mathbf{r})\mathbf{E}(\mathbf{r},\mathrm{t})] = 0 \\ \boldsymbol{\nabla}\times\mathbf{H}(\mathbf{r},\mathrm{t}) - \epsilon_0\epsilon(\mathbf{r})\frac{\mathbf{E}(\mathbf{r},\mathrm{t})}{\partial t} \\ \boldsymbol{\nabla}.\mathbf{H}(\mathbf{r},\mathrm{t}) = 0 \\ \boldsymbol{\nabla}\times\mathbf{E}(\mathbf{r},\mathrm{t}) + \mu_0\frac{\partial\mathbf{H}(\mathbf{r},\mathrm{t})}{\partial t} = 0 \end{gathered} \tag{2.63}$$

By inserting harmonic time dependent fields in the form of $\mathbf{H}(\mathbf{r},\mathrm{t}) = \mathbf{H}(\mathbf{r})e^{-i\omega t}$ and $\mathbf{E}(\mathbf{r},\mathrm{t}) = \mathbf{E}(\mathbf{r})e^{-i\omega t}$ into equation (2.63), following equations are obtained

$$\boldsymbol{\nabla}.[\epsilon(\mathbf{r})\mathbf{E}(\mathbf{r})] = 0 \text{ and } \boldsymbol{\nabla}.\mathbf{H}(\mathbf{r}) = 0 \tag{2.64}$$

$$\boldsymbol{\nabla}\times\mathbf{H}(\mathbf{r}) - i\omega\epsilon_0\epsilon(\mathbf{r})\mathbf{E}(\mathbf{r}) \tag{2.65}$$

$$\boldsymbol{\nabla}\times\mathbf{E}(\mathbf{r}) - i\omega\mu_0\mathbf{H}(\mathbf{r}) = 0 \tag{2.66}$$

Divide both side of equation in (2.65) and take curl of the both sides, then use equation (2.66) to eliminate $\mathbf{E}(\mathbf{r})$ term. The resultant equation is

$$\nabla\times\left(\frac{1}{\epsilon(\boldsymbol{r})}\nabla\times\mathbf{H}(\mathbf{r})\right) = \left(\frac{\omega}{c}\right)^2\mathbf{H}(\mathbf{r}) \tag{2.67}$$

where c is the vacuum speed of light $\left(c = 1/\sqrt{\epsilon_0\mu_0}\right)$.

In order to find the modes $\mathbf{H}(\mathbf{r})$ corresponding frequencies, equation (2.67) should be solved for given $\epsilon(\boldsymbol{r})$.

Most FDTD solvers use central difference for finite difference. Although, it is possible to apply higher order approximations, 2nd order approximation is preferable and more convenient [30]. The 2nd order central difference approximation is given by

$$\left.\frac{df(x)}{dx}\right|_{x=x_0} \approx \frac{f\left(x_0+\frac{\delta}{2}\right)-f(x_0-\frac{\delta}{2})}{\delta} \tag{2.68}$$

Since central difference have 2nd order accuracy, error in the approximation decreases as least square of the reduced δ [30].

For TM waves, finite difference can be written as,

$$E_z^{n+1}(i,j) = E_z^n(i,j) + Z\frac{\Delta\tau}{\Delta x}\left[H_z^{n+\frac{1}{2}}\left(i+\frac{1}{2},j\right) - H_y^{n+\frac{1}{2}}\left(i-\frac{1}{2},j\right)\right] - Z\frac{\Delta\tau}{\Delta x}\left[H_z^{n+\frac{1}{2}}\left(i,j+\frac{1}{2}\right) - H_y^{n+\frac{1}{2}}\left(i,j-\frac{1}{2}\right)\right] \tag{2.69}$$

$$H_x^{n+\frac{1}{2}}\left(i,j+\frac{1}{2}\right) = H_x^{n-\frac{1}{2}}\left(i,j+\frac{1}{2}\right) - \frac{1}{Z}\frac{\Delta\tau}{\Delta y}[E_z^n(i,j+1) - E_z^n(i,j)] \tag{2.70}$$

$$H_y^{n+\frac{1}{2}}\left(i+\frac{1}{2},j\right) = H_y^{n-\frac{1}{2}}\left(i+\frac{1}{2},j\right) - \frac{1}{Z}\frac{\Delta\tau}{\Delta x}[E_z^n(i+1,j) - E_z^n(i,j)] \tag{2.71}$$

where $\tau = ct = \sqrt{\frac{1}{\mu\epsilon}}t$ and $Z = \sqrt{\frac{\mu}{\epsilon}}$.

After this point, FDTD method can be explained in some basic steps. First stage both electric and magnetic field in time and space is by replacing all derivatives with finite differences and discretizing time and space. Then solve these difference equations to get "update equations" new unknowns in terms of past (known) fields. The next step is to evaluate electric and magnetic fields one step further. Finally, repeat the previous step until the fields are obtained over the desired direction.

2.7 Ellipsometry

Elipsometry is a technique that provides information about dielectric properties of a thin film. Polarization properties of the reflected light depend on the angle of incidence, polarization direction of the incident light, and the reflection properties of the surface under the influence of the refractive index. Elipsometer measures chance in these polarization properties.

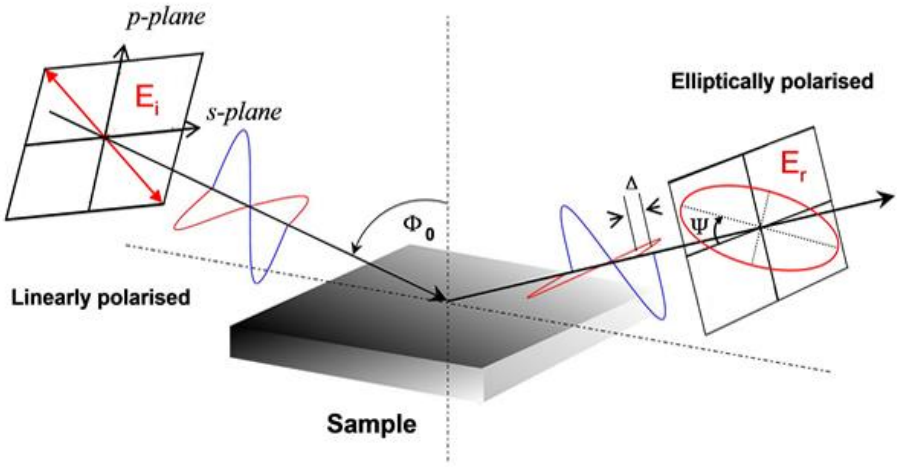

Figure 2.9 Elipsometer configuration

A linearly polarized incident beam becomes elliptically polarized after reflection. Shape and orientation of the ellipse provides information about reflecting surface. Resultant data is given in terms of relative phase (Δ) change and relative amplitude (Ψ) change. Δ and Ψ are not directly physical data, but they can be related to reflectivity by

$$\frac{r_p}{r_s} = e^{i\Delta} \tan \Psi \tag{2.72}$$

where r_p and r_s are p-polarized and s-polarized complex reflectivity components respectively. When it comes to analysis part, equation (2.42) is not very easy to solve so numerical calculations are used with models such as Cauchy model and Lorentz model.

Cauchy Model

Cauchy model is mostly used for transparent materials. Cauchy relation is

$$n(\lambda) = A + \frac{B}{\lambda^2} + \frac{C}{\lambda^3} \tag{2.73}$$

where $n(\lambda)$ is refractive index as function of wavelength (λ). Since Cauchy model is not constrained by Kramers-Kronig relations, it can give unphysical dispersions. Transparent wavelength region of some absorber could be modeled with Cauchy but it is usually not preferred. Lorentz, Gaussian, Harmonic oscillator models are more acceptable for absorbing materials.

Lorentz Model

For absorbing materials refractive index has both real and imaginary parts in absorbing region. With Kramers-Kronig consistency used for real part, imaginary part is treated like an oscillator. Lorenz oscillator model relation is

$$\boldsymbol{\epsilon} = \epsilon_{1,\infty} + \frac{AE_c}{E_c^2 - E^2 - iBE} \tag{2.74}$$

where A is the amplitude, B is the broadening and E_c is the central energy of Lorenz oscillator. In addition $\epsilon_{1,\infty}$ is real part of the dielectric function for very large photon energies.

Effective Medium Approximation (EMA)

The optical functions of thin films are modeled by EMA via using an average of two or more different sets of optical functions. The approach used to carry out the average is important. In order to that, a composite or effective medium dielectric function should be found for the whole film based on the dielectric functions of two or more other materials. The most common EMA theory can be expressed

$$\frac{\langle\epsilon\rangle - \epsilon_h}{\langle\epsilon\rangle - \gamma\epsilon_h} = \sum_i f_i \frac{\epsilon_i - \epsilon_h}{\epsilon_i - \gamma\epsilon_h} \tag{2.75}$$

where $\langle\epsilon\rangle$ is the dielectric function of the effective medium, ϵ_h is the dielectric function of the host, f_i is the fraction of the i^{th} component, and γ is a factor related to the screening and the shape of the inclusions (for example, $\gamma = 2$ for 3-dimensional spheres) [31].

Chapter 3

Experiments

Experimental part of the thesis consists of ellipsometric characterization of the active layer used for exciton-plasmon coupling, which is a polyvinlylalkohol (PVA) thin film containing self-assembled cyanine dye molecules. The cyanine dyes that are used as excitonic sources during this study are represented by Lorentz oscillator model in FDTD simulations. In order to define Lorentz absorber parameters in the model, optical constants of cyanine thin film is required. After spin coating thin films of cyanine dye-PVA on silicon substrates, the optical constants of the thin films have been measured using variable angle spectroscopic ellipsometry technique.

3.1 Ellipsometric characterization of Cyanine dye thin films

Samples which were used in ellipsometric measurements are prepared on 380±15μm Silicon wafer. Si wafer was first degreased and then cleaned in piranha's solution (30% H_2SO_4, H_2O_2 (3:1)). Polyvinyl alcohol suspension is heated to 150 ° C for half an hour to dissolve the PVA in water to obtain 5% PVA solution. Cyanine dye (TDBC - 5,5',6,6' – tetrachloro - di - (4 - sulfobutyl) - benzimidazolocarbocyanine) molecules were also dissolved in water. These two solutions are mixed in 1:1 (v:v) ratio to obtain 0.75% PVA with known concentration of cyanine dye in water. The homogenous TDBC-PVA solution was spin coated on a silicon substrate with the spinning parameters of, firstly for 5 seconds 500 rpm and, secondly for 30 seconds 3000 rpm.

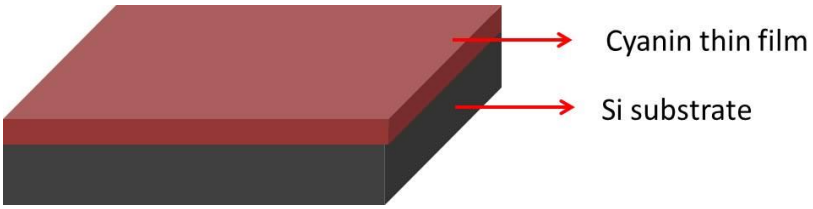

Figure 3.1 TDBC-PVA thin film coated on a Si substrate having a native oxide layer on it. The Si substrate is cleaned before coating active layer in order to remove the Si wafers surface of all foreign objects, such as dirth, silicon particles and dust.

Thickness of the resultant film was around 350 nm. Four different samples were prepared from 5mM, 2.5 mM, 1.3 mM and 0.6 mM molarities of TDBC in 5% PVA solutions and spin coated on silicon wafers as shown in Figure 3.**1**. Thin films of TDBC/PVA with different concentration of TDBC molecules were characterized using the spectroscopic ellipsometer.

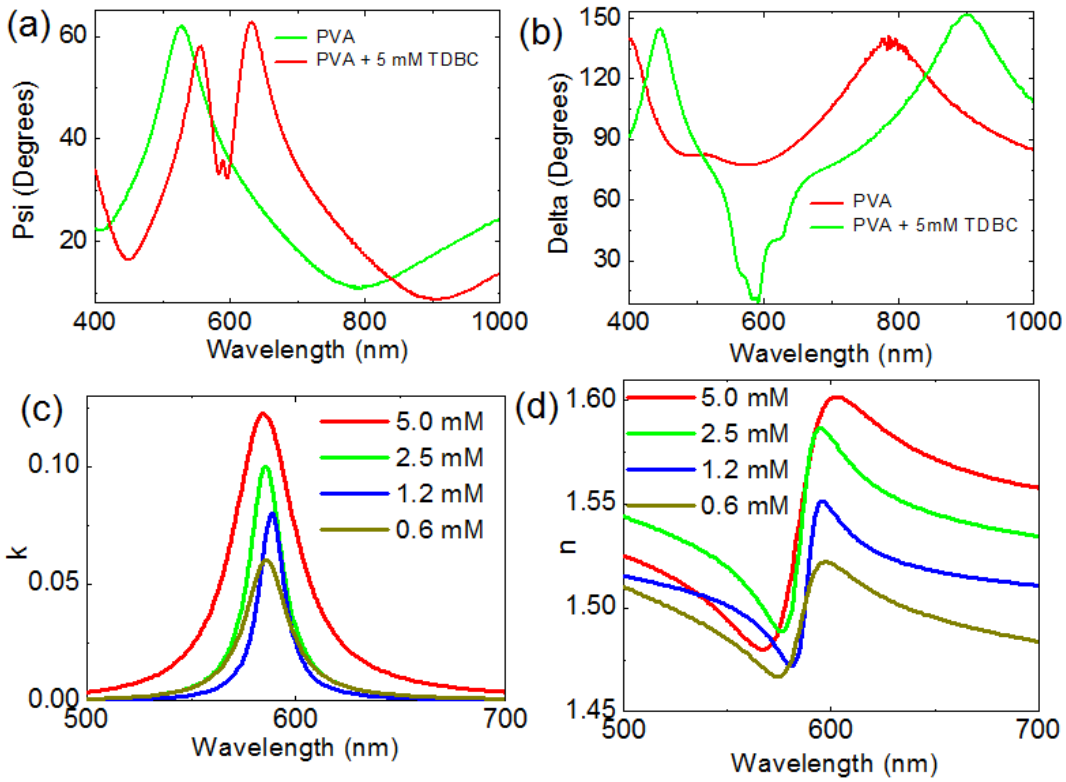

Figure 3.2: Optical constants of TDBC in the PVA matrix. Psi (a) and Delta (b) values of the PVA film and 5 mM TDBC molecules in the PVA matrix, respectively. The PVA solution, containing 5% PVA in water, was spin-coated on a silicon wafer. Spinning parameters of the PVA film were 5 seconds at 500 rpm and then 30 seconds at 3000 rpm. The thickness of the fabricated polymer film containing the TDBC molecules in the PVA matrix is around 350 nm. (c) Extinction coefficient (k) and (d)

refractive index (n) of the TDBC-PVA film as a function of wavelength for varying concentrations (5.0 mM, 2.5 mM, 1.2 mM and 0.6 mM) of the TDBC molecules in the PVA matrix.

Optical constants, the extinction coefficient (*k*) and the refractive index (*n*) of TDBC molecules/PVA mixture for different TDBC concentrations dissolved in the PVA matrix using variable angle spectroscopic ellipsometer (VASE) were measured, [Figure 3.2]. The refractive index of transparent materials is often described using Cauchy relationship, which is described as: $n(\lambda) = A + B/\lambda^2 + C/\lambda^3$ where the three terms are adjusted to fit the refractive index of the transparent materials as a function of wavelength to the experimental data. However, when the material is not transparent and thus absorbing, Lorentz oscillator model can be used to describe the optical constants of the material as a function of wavelength. The Lorentz oscillator is written as $\epsilon = \epsilon_{1,\infty} + AE_c/E_c^2 - E^2 - iBE$ where *A*, *B*, E_c, ϵ are amplitude, broadening, center energy and background dielectric constant, respectively. Spectroscopic ellipsometer measures the complex Fresnel reflection coefficient ratio for s- and p-polarized incident light as a function of the wavelength of the light for a given incidence angle. The Fresnel reflection coefficients ratio is defined as $\rho = \frac{r_p}{r_s} = \left|\frac{r_p}{r_s}\right| e^{i\Delta_p - \Delta_s} = \tan(\Psi)\, e^{i\Delta}$ in which Δ (delta) and Ψ (psi) are the ellipsometric angles giving the changes in the magnitude and phase of the incident light after reflection from an optical film. r_p and r_s are p- and s-polarized Fresnel reflection coefficients, respectively. The measured psi and delta values for the bare PVA film and TDBC containing PVA film are given in Figure 3.2. These values can be used to measure optical properties of the studied material. In order to calculate the optical constants of the coated TDBC/PVA blend on Si substrate, effective medium approximation (EMA) model was used. In this model, Cauchy and Lorentz models are coupled to each other. Thicknesses of the prepared films were found to be in the range of between 300 nm and 360 nm. Calculated *n* and *k* values of TDBC/PVA blend film with varying TDBC concentration on Si wafers are shown in Figure 3.2c and Figure 3.2d, respectively.

CHAPTER 4

Simulations of exciton-plasmon coupling

In this part of the thesis, theoretical investigation of exciton-plasmon coupling on plasmonic surfaces using FDTD simulations is reported. The simulations are performed for flat surfaces, uniform gratings and Moiré surfaces. In the first part of the chapter, FDTD simulation technique is introduced in detail. The effects of varying the thickness of the plasmonic layer and optical density of the J-aggregate dye molecules located on the plasmonic surface on the exciton-plasmon coupling is studied. J-aggregate dye molecules are placed inside plasmonic band gap structures as the excitonic source to understand the behavior of J-aggregate dye molecules inside a plasmonic band gap. It was found that, by altering periodicity and grating depth of the uniform grating, resonance condition of exciton- plasmon coupling can be controlled. In the final part of this chapter, J-aggregate dye molecules are placed in a plasmonic cavities and exciton-plasmon coupling is studied.

4.1 Simulations of exciton-plasmon coupling with FDTD method

Plasmons are collective oscillations of the free electron gas density at certain frequencies and a plasmon is a quantum of plasma oscillation just as a photon is the quantum of light. Excitons are bound states of an electron and a hole, which are attracted to each other by electrostatic forces and can be defined as quasiparticles with complex index of refraction allowing us to model exciton-plasmon coupling using electromagnetic theory. There are various methods to numerically solve the

relevant equations for exciton-plasmon coupling, for example, transfer matrix method, finite difference time domain (FDTD) simulation method. In this work, FDTD method is used via Lumerical FDTD Solutions software package (Figure 4.1) to numerically investigate exciton-plasmon coupling. Lumerical software package allows us to model and simulate various photonic structures. Although there are many similar software packages used for simulation of photonic structures, this particular one has a strong scripting engine which makes optimization and sweep of random parameters possible. For instance, in order to build a plasmon dispersion curve, we have to sweep the incidence angle and wavelength of the incident light with high resolution. In that, a wavelength sweep should be done for each angle, thus a simple code including two nested "for" loops successfully does the sweeping. Although Lumerical has its own sweeping function, it doesn't allow us to utilize such an easy nested sweep.

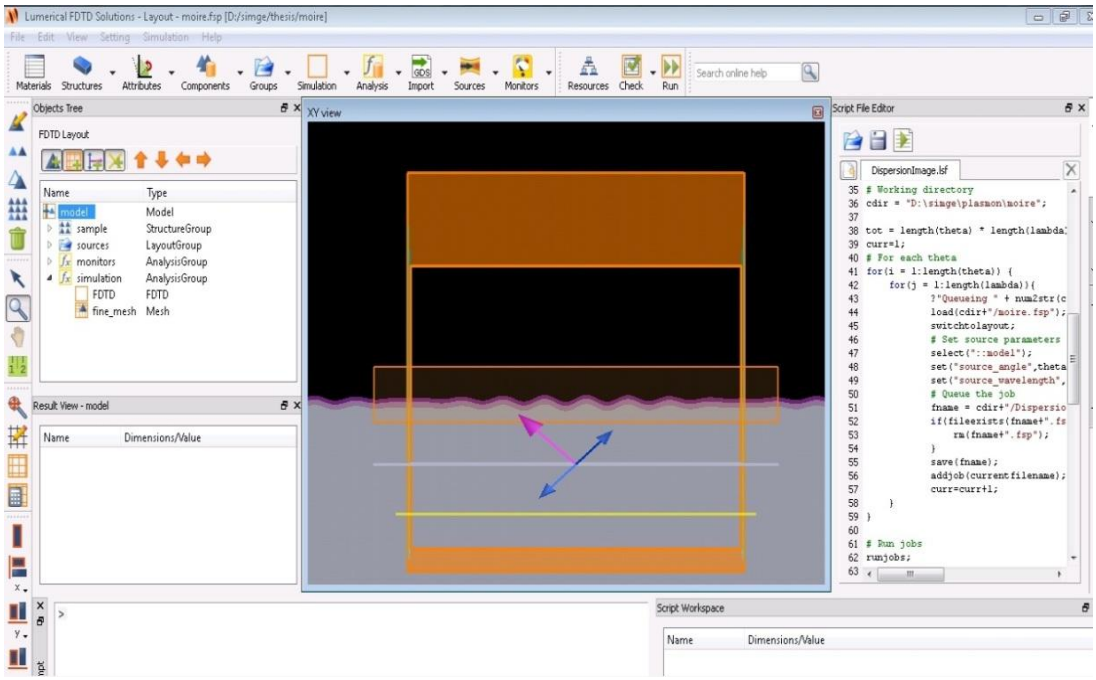

Figure 4.1 Graphical user interface of the Lumerical FDTD solutions software

Since FDTD method is a fully vectorial method, it is possible to simulate a 3D object. However, simulation of an actual sample in 3D would take longer computation hours than simulation of a 2D object. Instead, we do some approximations during our FDTD simulations. First of all, we assume that our

structure is infinitely uniform in one direction (usually marked as z-axis), and thus calculations in this direction are ignored and the problem is turned into a 2D problem. Then, a second approximation is made by using periodic boundary conditions in horizontal direction (usually marked as x-axis); here we assume that our pattern repeats infinitely, hence, we ignore the edge effects. These are the basic approximations we make for each structure. Each individual structure might have different points to be considered and will be mentioned when they are described. Lumerical software package has its own simulation methodology. Although main functionality is similar to its other simulation packages, this software package has its own language.

In the simulation window, a structure group, collection of optical materials that are investigated, is defined. In our case, there are three main structures with different optical properties. One is the substrate that supports the plasmonic layer and generally soda-lime glass is used for this purpose. A metal thin film coated on a glass substrate is added. Thin layer of metal on a glass substrate supports propagation of surface plasmons between metal and dielectric interface. In our case, the metal is usually silver (Ag). Optical properties of Ag are extracted from Palik's handbook [32]. Silver is the most common plasmonic meteal and it has superior plasmonic properties in the visible part of the electromagnetic spectrum. On top of the plasmonic layer, an absorbing dielectric layer consisting of a polymer thin film and exciton source is located. Optical properties of J-aggregate dye molecules used as the exciton source embedded in polyvinyl alcohol (PVA) thin film have been obtained by spectroscopic ellipsometry measurements (See Ch.3). Glass substrate, metal layer and absorbing dielectric layer can be placed in simulation window with controllable thickness and material type. In the simulation window, these structures can be turned on or off and their surfaces can be modified, if needed.

Light source is defined as a plane wave source that is placed below the structure interface. The injection axis of the source and direction, angle, wavelength and polarization are all defined in the model script. Reflection and transmission response of the structure is measured by a power monitor that is placed under the plane wave

source. A power monitor records the amplitude of the reflected field that passes through itself and, from these; it calculates the Poynting vector and the total power. In the end, total power recorded by the monitor is normalized with respect to the source power. Measurement of reflection or transmission depends on where this power monitor is placed. Since light source is also under the sample, if the power monitor is placed under the sample, it measures the power reflected from the sample hence normalization gives the reflection response; if it is placed over the sample, it gives the transmission response.

Simulations must be restricted to a simulation window. Since we use periodic structures as well as flat metal surfaces, width of the simulation window is set to a lateral width which corresponds to one period of the pattern. Bloch boundary conditions are applied at the lateral boundaries to force periodic boundary conditions. Thus structures behave like they are placed at the both ends of the area with infinite periodicity. Vertical boundaries are confined with several perfectly matching layers (PMLs) to prevent the monitor from erroneous readings due to unwanted reflections and refractions from the PML surfaces. Since only one PML layer cannot fully attenuate the whole field, some residual field power may remain. Width of the power and source monitor is fitted to simulation area to scan the entire region in the boundaries. There are also index and movie monitors to be used, if they are needed. By using the index monitor, one can measure the refractive index of the simulated structure and check whether the optical structures that are placed are in the right order or not. To get more accurate results, interface between metal and dielectric is fine meshed with a 6 nm mesh size. Simulation time is set as 200 femtoseconds, which is the time necessary for light to travel from one cell to another (see part 2.6.1). Simulation software has a parallel run choice for multi-processor/core systems. Our simulation software has 8 processors. In our case, for a basic simulation, software is scripted to define, create, run and analyze approximately 1500 files, and it takes at least 18 hours nonstop computation to fully complete a dispersion curve. Increasing simulation time, simulation area, mesh size and sweep parameters extend computation time. We created our own control panel with the

variables as shown in Figure 4.2. Some other properties of the calculation which are constant for every simulation are defined in script panel of the software.

User properties

Name	Type	Value	Units
source_angle	Number	46	
source_wavelen...	Length	0,627	microns
index_monitor_...	Number	0	
movie_monitor...	Number	0	
period1	Number	0,267	
period2	Number	0,303	
sample_length	Length	5	microns
grating_depth	Number	0,04	
substrate_thick...	Number	1	
substrate_mater...	Material	SiO2 (Glass) - P...	
substrate_index	Number	1,44	
layer1_on	Number	1	
layer1_thickness	Number	0,04	
layer1_material	Material	Ag (Silver) - CRC	
layer1_index	Number	1,44	
layer2_on	Number	1	
layer2_thickness	Number	0,03	
layer2_material	Material	J-Aggragate - B...	
layer2_index	Number	1,55	

Figure 4.2 Control panel with variables used during simulation

Here “Number” is unitless numerical value and “Length” is a numerical value whose unit is in micrometers. Dispersion curves are obtained in Kretschmann configuration during the simulation of exciton-plasmon coupling. First of all, we take reflection curve at a fixed incidence angle for a given range of wavelengths which is mostly in the visible region of the electromagnetic spectrum (Figure 4.3a). There is a dip in the reflection curve, which is due to excitation of surface plasmon polariton mode (SPP) on the surface. This happens when the incedent light resonates with the plasma

oscillations on the metal surface. Therefore, the incident light is coupled to the surface modes and does not reflect back. The excitation of SP on a flat metal surface through a prism has a Lorentzian shape spectrum which can be defined as $R(\omega) \propto \frac{\Gamma}{(\omega-\omega_0)^2+\Gamma^2}$. The damping term, Γ defines the linewidth of the reflection spectrum. The linewidth can be controlled by tuning the metal thickness, which determines the coupling, thus the damping of SPP's. ω_0 is the surface plasmon resonance frequency. The reflectivity goes to minima where the phase matching condition between the incident light and surface plasmon polariton is satisfied, Figure 4.3a. This is achieved when the horizontal component of the incident light k_x matches the real part momentum of SPP (k_{spp}). The dispersion relation of SPPs at a metal-dielectric interface can be defined as $k_x = k_0 n_p \sin(\theta) = k_{spp} = \frac{2\pi}{\lambda}\sqrt{\frac{\epsilon_m \epsilon_d}{\epsilon_m+\epsilon_d}}$ where λ is the wavelength of the incident light, k_0 is the free space wavevector of the incident light $\left(\frac{2\pi}{\lambda_0}\right)$, ϵ_m and ϵ_d are the dielectric constants of metal and dielectric, respectively, n_p is the refractive index of the prism, and n_p is the SPP resonance angle.

Reflection curves are obtained for incidence angles with a separation of approximately 0.2 degrees. Each wavelength corresponds to different energy, and by changing the incidence angle, we change the momentum of the incident light that is coupled to the SPP. Hence, by plotting the wavelength versus the angle, response of the surface reflectivity in a heat map, dispersion images can be obtained (Figure 4.3b).

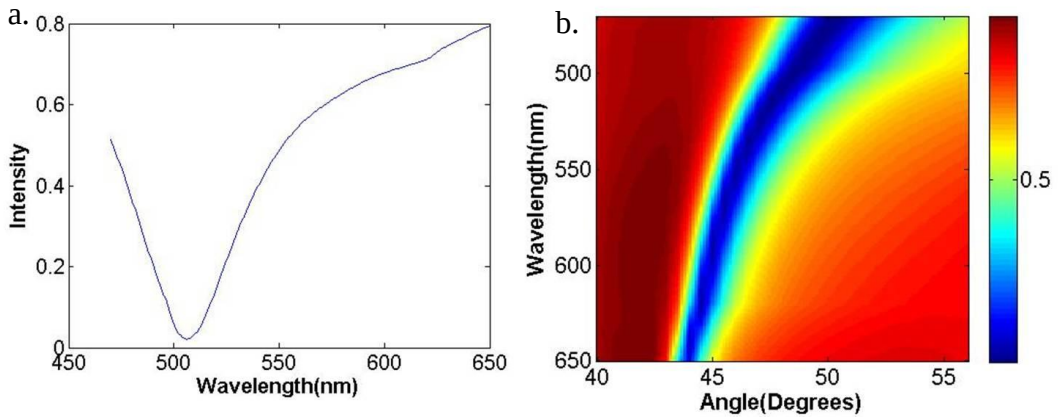

Figure 4.3 Dispersion curve for SPP on flat metal surface. (a) Surface plasmon resonance reflection spectrum. The dip in the spectrum shows the surface plasmon resonance wavelength at specified incidence angle. (b) SPP dispersion curve of a flat 40 nm thick Ag surface. The blue and red regions show the low reflectivity and high reflectivity regions, respectively.

A heat map is a two dimensional plot designed to represent a three dimensional data, where the third dimension is represented by colors. Here red represents maximum light intensity (reflection) and blue represents minimum light intensity (surface-plasmon polariton coupling). In the blue region, light couples with surface plasmons and then attenuates.

4.2 Exciton-plasmon coupling on flat metal surfaces

In order to tune exciton-plasmon coupling, simulations of exciton-plasmon coupling are performed on flat metal surfaces. In the simulation window, 30 nm thick J-aggregate film and 40 nm thick Ag film is placed on a glass substrate, respectively. Then dispersion curves are calculated.

In Figure 4.4, dark grey line is for the light source and arrow on the glass-substrate represents direction of the incoming light. The yellow line below the source is a power monitor that measures total power that goes through, then normalizes with respect to the source. First, we simulate the response of the flat metal surface without J-aggregate absorbing layer. The response of the flat metal surfaces to the incident light without any J- aggregate layer is shown in Figure 4.5.

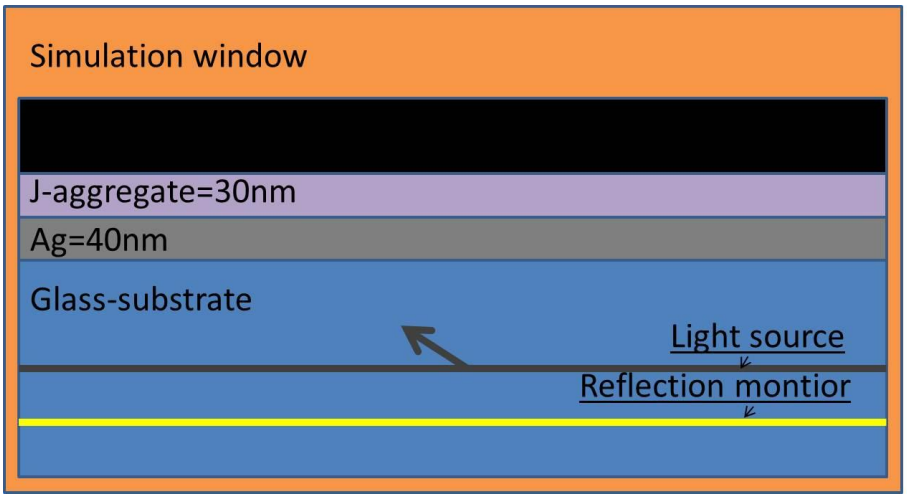

Figure 4.4 Simulation window of exciton-plasmon coupling on flat metal surfaces. The yellow line shows the reflection monitor placed at the bottom of the simulation window. The light source with an arrow indicating the incidence direction of the light is placed above the reflection monitor with a black line. Glass substrate is defined in blue colored region. A 40 nm thick Ag layer is located on top of the glass substrate to support propagation of surface plasmons. The absorbing J-aggregate dielectric layer is positioned above the metal layer to couple with the surface plasmons. The dark region above the J-aggregate layer shows the air.

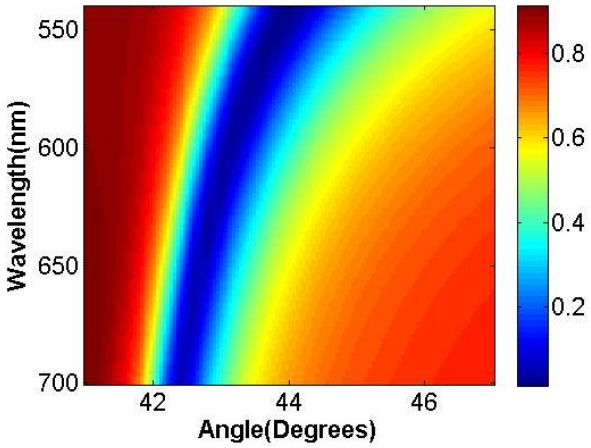

Figure 4.5 Dispersion curve for SPP coupling on flat metal surfaces. In the blue regions, incident light resonates with the surface plasmon. In the red regions, the incident light is reflected without coupling to surface plasmons**.**

The vertical axis represents the SPP energy while the horizontal axis represents the SPP momentum. The intensity scale is displayed next to the graph for reference. Here, we observe a blue band starting at around 42.5 degrees and extending to 44 degrees indicating the light that couples to the surface plasmons. Keeping in mind

that blue represents the minimum light reflected, the blue band is an indicator of the lower branch of the SPP dispersion curve for flat metal surfaces. This result is expected and is typical of flat surfaces. The observed dispersion on Figure 4.5 can also be better understood if we recall equation 2.43.

In order to monitor evolution of the exciton-plasmon (polariton) dispersion curves with the optical density of TDBC molecules, wavelength of the reflection dips as a function of the incidence light angle was acquired. After obtaining the response of bare flat metal surface to incident light, two different runs were carried out in order to introduce the effect of J-aggregate into the simulation. J-aggregate has strong absorption at around 590 nm and can be represented by a Lorentz oscillator whose strength can be adjusted. We also have the capability to adjust the metal film thickness. We suspect that the role of metal thickness in the formation of the SPPs and the exciton-plasmon interaction can be understood by tuning the metal thickness as well. Initially, Lorentz total oscillator strength was varied on flat metal surfaces while keeping the thickness of the metal constant. As stated in Sec. 4.1, Lorenz oscillator parameters are defined by using the data for optical constants, which is taken from the optical characterization of cyanine dye thin films. Since J-aggregates have complex index of refraction, they are modeled using a Lorenz oscillator. The Lorentz total oscillator strength can be defined as Lorentz permittivity which does not have any units. While Ag film thickness was fixed, Lorentz total oscillator strength (f) was changed from 0 to 0.5, this tuning range corresponds to 0.01 mM to 1 mM concentration of J-aggregated cyanine dye. Hence, the total oscillator strength of the J-aggregate can be tuned by varying the concentration of the J-aggregate. Note that this is only a practical choice; we didn't carry out the exact mapping between molarity and this arbitrary oscillator strength, since it wouldn't affect the calculations. We are just interested in the splitting behavior of the dispersion curve. Results of the simulation are shown in Figure 4.6.

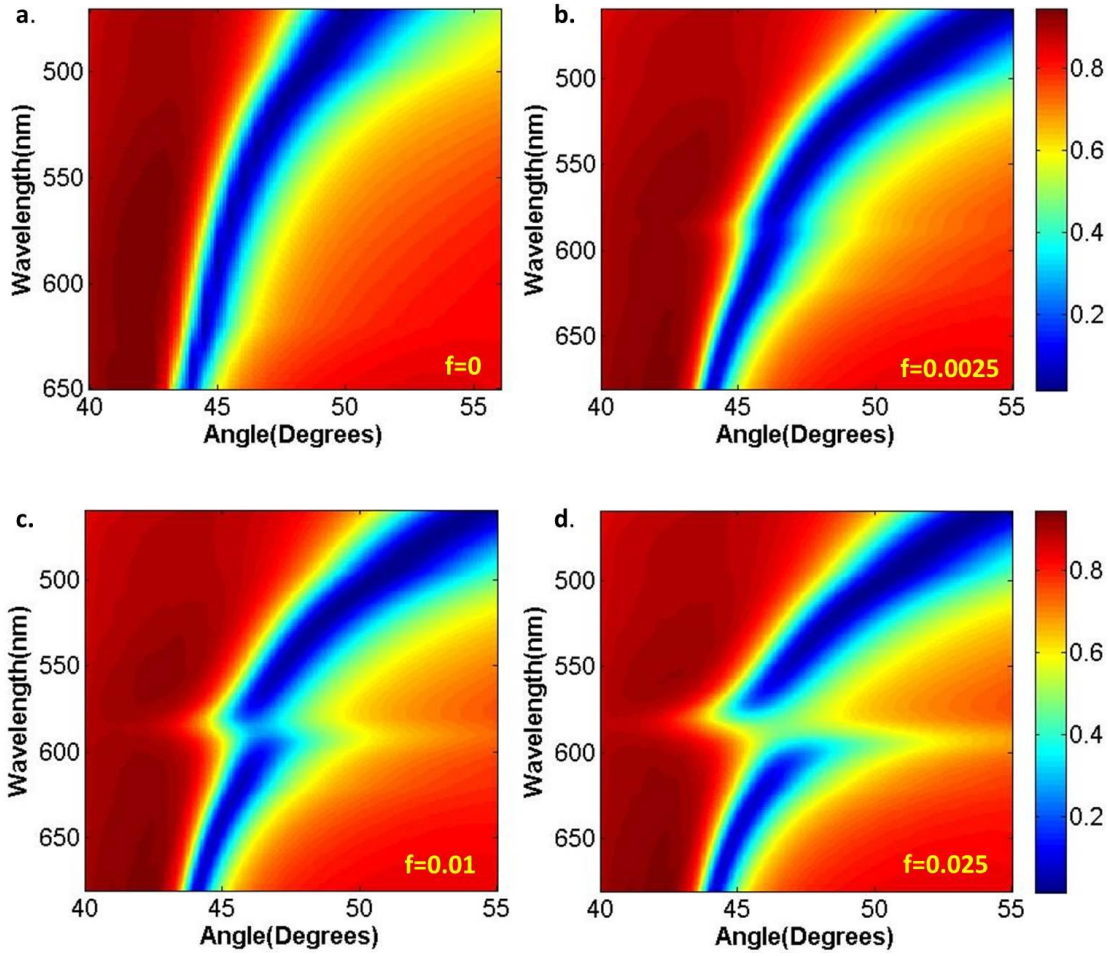

Figure 4.6 Exciton-plasmon coupling as a function of Lorentz total oscillator strength. Lorentz oscillator strengths are (a) 0, (b) 0.0025, (c) 0.01, and (d) 0.025.

The heat map shown in Figure 4.6a is very similar to the results obtained for bare flat metal surfaces since the Lorentz total oscillator strength is set to zero for this simulation. As we increase the Lorentz total oscillator strength (the concentration of J- aggregate molecules) we observe changes in the dispersion curve. First a kink forms at around 590 nm wavelength, which corresponds to the absorption peak of J-aggregate. The kink widens as the total oscillator strength increases and becomes pronounced at the oscillator strength of 0.01. The blue and red regions show reflection minima and maxima, respectively. It is worth mentioning here that without TDBC molecules placed on the plasmonic layer, the SPP reflection curve do not show any anti-crossing peaks characteristic of plasmon-exciton coupling. It is clear from Figure 4.6d the threshold for Rabi splitting is reached when the total oscillator

strength reaches to 0.025. This indicates that the system is under strong coupling regime leading to anti-crossing of plasmon and exciton responses. Upon further increase, the distorted dispersion curve separates and a gap opens up at around the same wavelength of 590 nm (2.1eV). At Rabi splitting angle where bare exciton and bare plasmon energies meet, reflection spectra demonstrate increase of the separation between the lower and upper polariton branches as a function of concentration as described by equation 2.62. Enhancement of the Rabi splitting with concentration of the TDBC molecules is due to the increase in the optical density of the J-aggregate film and therefore increase in total oscillator strength. For a specific absorbing material, the Rabi splitting between the plasmonic state and the excitonic state is expected to vary as $(\alpha_0 L)^{1/2}$, where α_0 is the peak absorption coefficient and L is the absorbing material film thickness [33].

When we continue to increase Lorentz oscillator strength, the splitting of the SPP branch increases and the Rabi gap follows. Further increase in oscillator strength a new state starts to appear besides the widening in splitting (Figure 4.7). As clearly seen in Figure 4.6 and 4.7, Rabi splitting increases with the increase in Lorentz oscillator strength. After certain amount of oscillator strength, possibly, due to strong absorption, a faint new state becomes visible at wavelengths that correspond to absorption wavelength of J-aggregate. This faint new state with weak dispersion may either be a localized mode or a pure excitonic state suggesting the localization of exciton-plasmon hybrid mode.

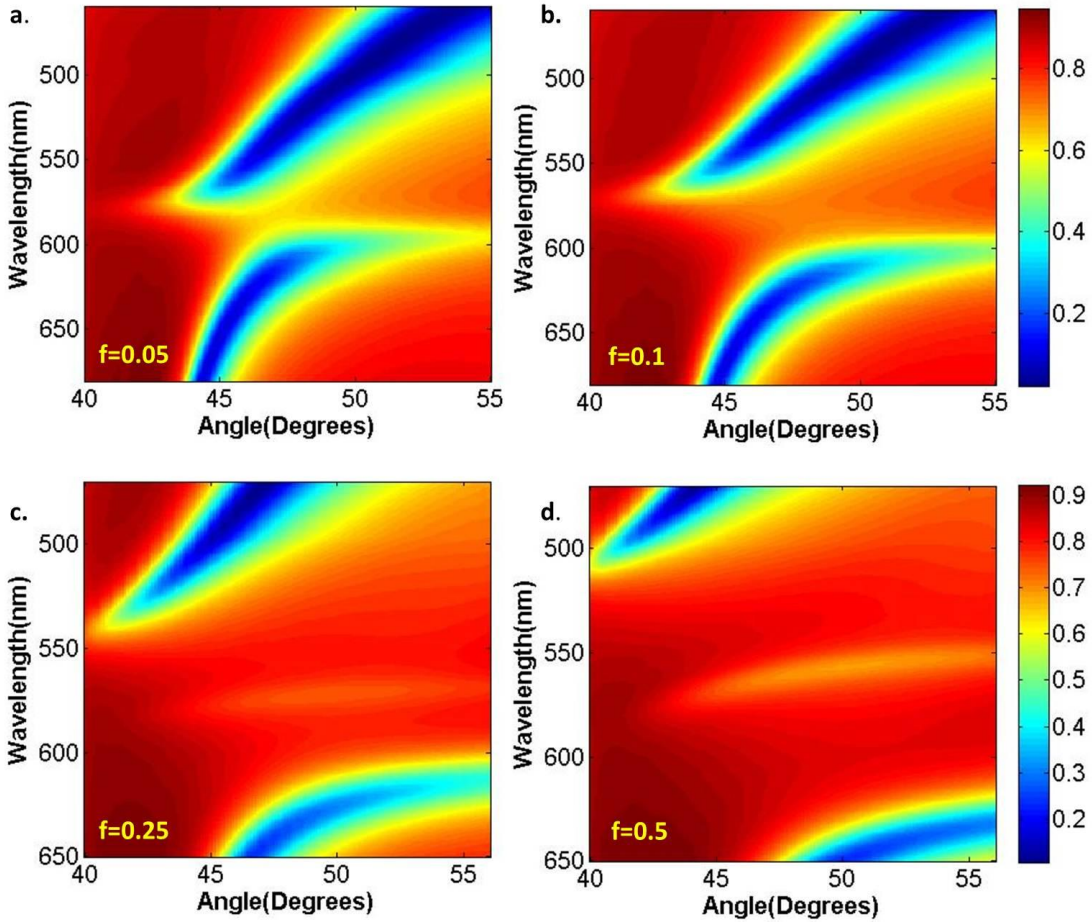

Figure 4.7 Exciton-plasmon coupling as a function of Lorentz oscillator strength. The Lorentz oscillator strengths are (a) 0.05, (b) 0.1, (c) 0.25, and (d) 0.5.

After varying Lorentz oscillator strength of the J-aggregate, metal film thickness is another parameter to be varied. In this case, dye layer thickness and the concentration of dye molecules (Lorentz oscillator strength) is fixed at 0.1. We vary the Ag film thickness (t) from 20 nm to 50 nm in steps of 5 nm. Dispersion spectra obtained in this way are shown in Figure 4.8. As shown in Figure 4.8a, two intense blue regions are localized with a separtion between them. There is a weak minima in blue at the absorption wavelength, 590 nm, for the 25 nm thick metal with j-aggregate. For the metal with 30 nm thickness, a gap clearly opens up, Rabi splitting. While increasing metal thickness, separation between Rabi energies also increases (see sec.2.4.2). Increase in the separation can be clearly seen in Figure 4.9. Increasing metal thickness further than 40 nm also results with increase in the separation, but intensity of the light at the upper and lower branches start to decrease (Figure 4.10).

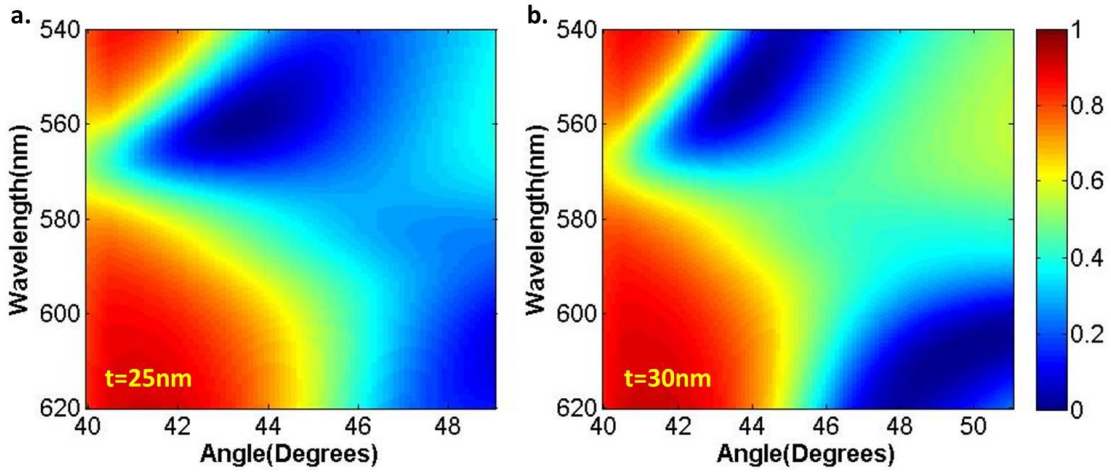

Figure 4.8 Tuning exciton-plasmon coupling on flat metallic thin film as a function of metal thickness (t). The metal film thicknesses are (a) 25 nm and (b) 30 nm.

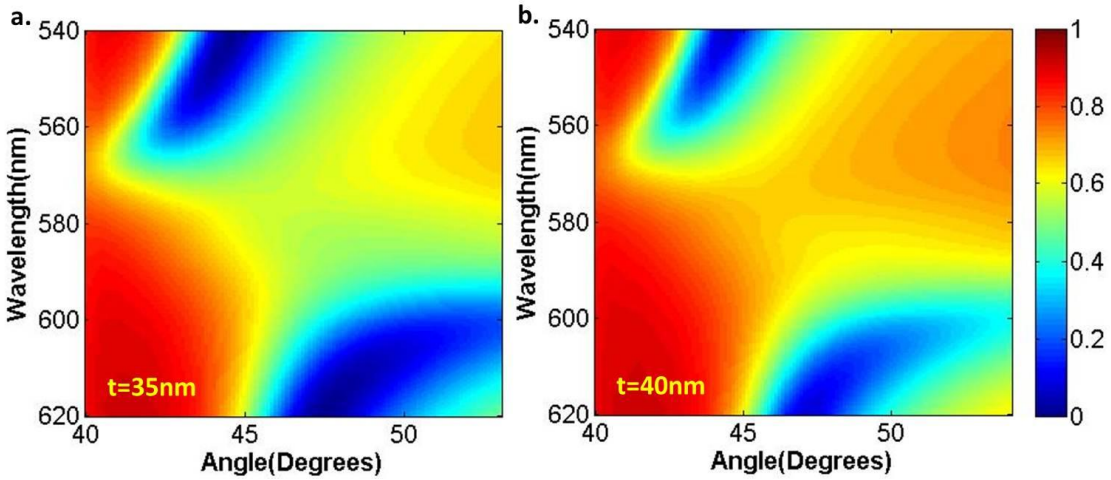

Figure 4.9 Tuning exciton-plasmon coupling on flat metallic thin film as a function of metal thickness (t). The metal film thicknesses are (a) 35 nm and (b) 40 nm.

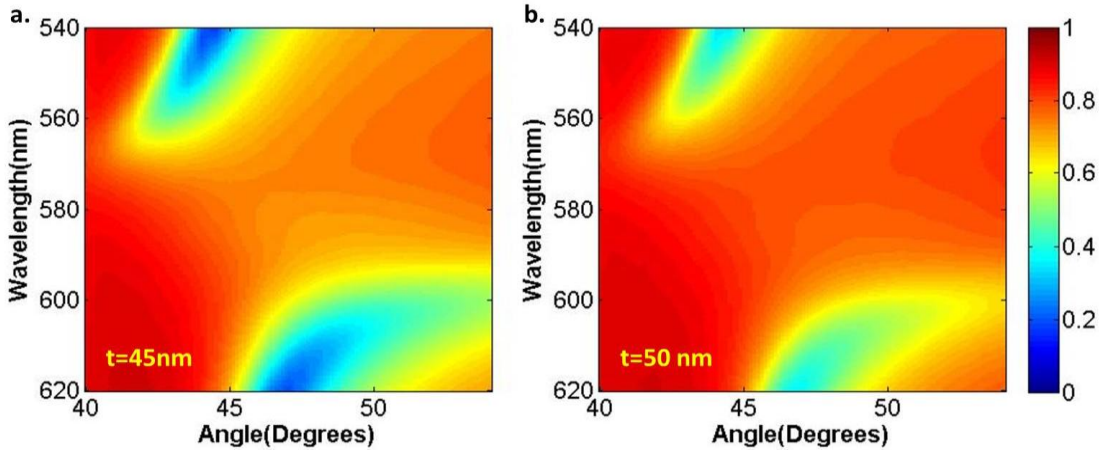

Figure 4.10 Plasmon-exciton coupling on flat metallic thin film as a function of metal thickness (t). The metal film thicknesses are (a) 45 nm and (b) 50 nm.

Let us look at the details of plasmon-exciton interaction on the metal surface to understand correlation between the Rabi splitting and damping of the surface plasmon resonance. The dipole moment of TDBC molecules coated on the silver surface interacts with the electric field of SPPs. The coupling energy between the SPP and TDBC molecules is $\boldsymbol{E} = \vec{\boldsymbol{\mu}} \cdot \vec{\boldsymbol{E}}$, where $\vec{\boldsymbol{\mu}}$ the dipole moment of the material is, and $\vec{\boldsymbol{E}}$ is the electric field generated by the plasmons. Energy transfer rate between plasmon and exciton can be given as $\boldsymbol{g} = \boldsymbol{E}/\hbar$. At resonance condition, the two normal modes of the coupled oscillator without damping is $\boldsymbol{s_{\pm}} = \boldsymbol{A}\,\boldsymbol{\cos}(\boldsymbol{\omega_{ex}} \pm \boldsymbol{g})\boldsymbol{t}$ in which $\boldsymbol{g} = \boldsymbol{V_0}/\hbar$ is the energy transfer rate and $\boldsymbol{\omega_{ex}}$ is the excitonic transition frequency [34]. Given the plasmon mode damping and $\boldsymbol{\gamma_p}$ the exciton damping $\boldsymbol{\gamma_e}$ the two normal modes are now damped oscillations in time as $\boldsymbol{S_{\pm}} = \boldsymbol{Ae^{-(\kappa+\gamma)t/2}}\,\boldsymbol{\cos}(\boldsymbol{\omega_{ex}} \pm \boldsymbol{g'})\boldsymbol{t}$ where. $\boldsymbol{g'} = \sqrt{\left(\frac{V_0}{\hbar}\right)^2 - \frac{1}{4}\left(\boldsymbol{\gamma_p} - \boldsymbol{\gamma_e}\right)^2}$ It is obvious that matching $\boldsymbol{\gamma_p}$ and $\boldsymbol{\gamma_e}$ maximizes the coupling and therefore the Rabi splitting energy. We measured damping of SPPs, $\boldsymbol{\gamma_p}$, and the excitons, $\boldsymbol{\gamma_e}$, using the reflectivity and ellipsometry measurements, respectively. Since plasmon mode damping is inversely proportional to the plasmon lifetime ($1/\boldsymbol{\gamma_p}$), change in plasmon mode damping affects the energy transfer rate and hence the Rabi splitting energy [28]. Using coupled oscillator model, the energies of the polaritonic branches of the coupled oscillator system can be defined as $\boldsymbol{E_{1,2}(k)} = \frac{1}{2}\left[\boldsymbol{E_{spp}(k)} + \boldsymbol{E_{ex}}\right] \mp$

$\frac{1}{2}\sqrt{(\hbar\Omega_R)^2 + \left(E_{spp}(k) - E_{ex}\right)^2}$ in sec. 2.4.2. It is clear in Figure 4.10 that as the metal film thickness increases Rabi Splitting increases. Furthermore, Rabi splitting as a function of damping of the plasmonic mode can be analytically calculated [35].

4.3 Exciton-plasmon coupling on uniform gratings

In order to understand what happens when an exciton is placed inside a plasmonic band gap, a thin layer of J-aggregate is coated on a uniform grating. Exciton-plasmon coupling on uniform gratings is modeled. It is worth noting here that uniform gratings show plasmonic band gaps. To support propagation of surface plasmons, Ag thin film is placed between J-Aggregate layer and glass substrate. Surfaces are patterned with a sine function to obtain a uniform grating. Light source is represented by a dark gray line in Figure 4.11 where the arrow shows direction of the incoming light. The yellow line below the source is a power monitor that measures the incident field power by normalizing with respect to the source. The simulation schematic is completed with the simulation window, which has Bloch boundaries on lateral axis and several perfectly matching layers (PML) on vertical axis as in the previous case.

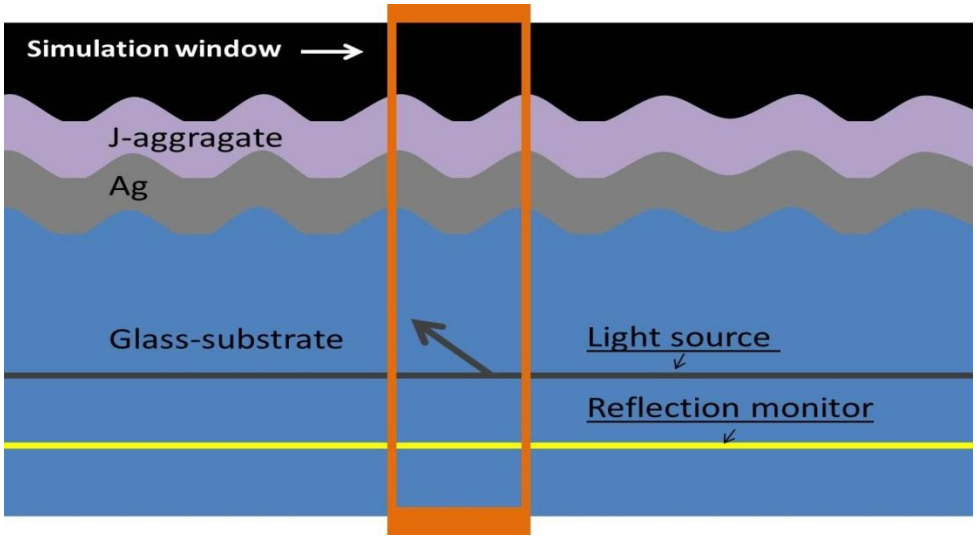

Figure 4.11 Simulation window of exciton-plasmon coupling on uniform gratings

Exciton-plasmon coupling on uniform gratings is investigated by varying periodicity and depth of the uniform gratings.

We start by characterizing the bare grating. J-aggregate layer is ignored and the response of the bare uniform gratings to the incident field is studied. Results of the periodicity response of the bare uniform gratings are shown in Figure 4.12 and 13.

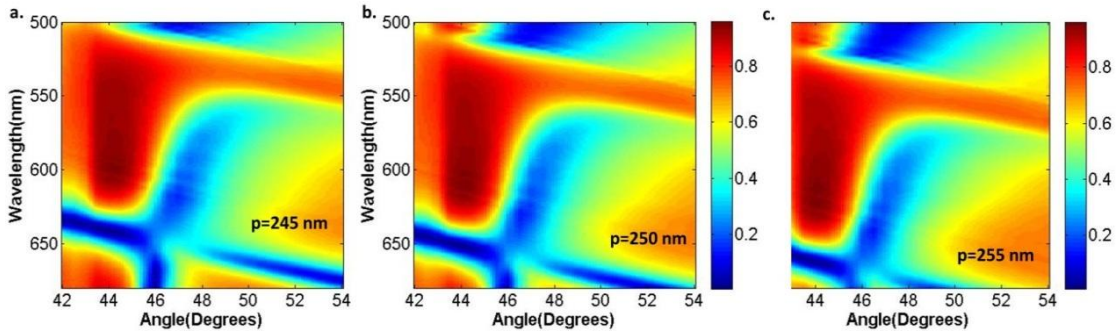

Figure 4.12 Dispersion curves for SPP on uniform gratings with different periods (p). The periods of the uniform gratings are (a) 245 nm, (b) 250 nm and (c) 255 nm.

Periodicity of the gratings was gradually changed from 245 nm to 255 nm with 5 nm separation. We start with a periodicity of 255 nm where we observe a gap in the dispersion of the uniform grating. There occurs a plasmonic band gap at the wavelength which is nearly twice the periodicity of the uniform grating structure.

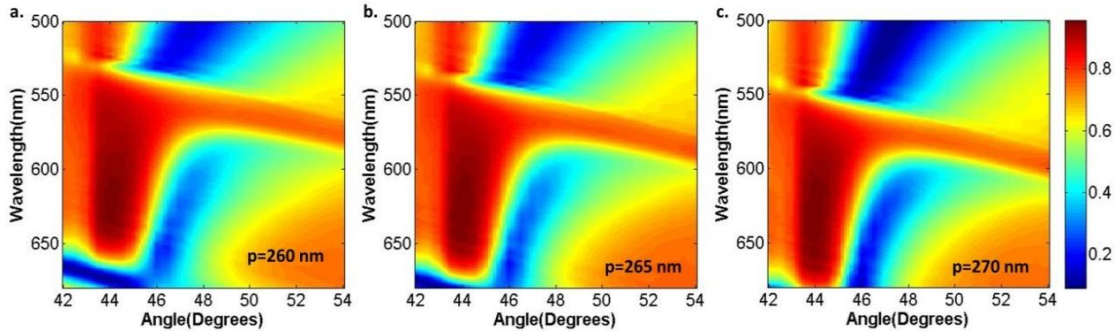

Figure 4.13 Dispersion curves for SPP on uniform gratings with different periods(p). The periods of the uniform gratings are (a) 260 nm, (b) 265 nm and (c) 270 nm.

As shown in Figure 4.12 and 13 band gap shifts to the red when the periodicity of the uniform grating is increased. As a result of this shift, the wave guide mode which can be easily seen in Figure 4.12a, down shifts and becomes invisible in Figure 4.13c.

The effect of periodicity on the exciton-plasmon coupling on the uniform gratings is studied in detail. Periodicity of the uniform grating is changed from 245 nm to 300 nm with 5 nm intervals while grating depth and plasmonic layer thicknesses are kept constant. Changing the periodicity of the uniform grating tunes the plasmonic bang

gap location. If a J-aggregate layer is added on top of the uniform grating structure, depending on the position of the band gap, absorption of the J-aggregate splits to either upper or lower edge of the gap. If the gap is not strong, it may even split both. As shown in Figure 4.14 and 4.15, splitting shifts with the periodicity of the uniform grating. Furthermore, there occurs a splitting due to exciton-plasmon coupling in the band gap of the uniform grating with a period of 255nm as shown in Figure 4.14. Although density of plasmonic states is very low in the band gap, when absorption line of the j-aggregate matches with the band gap, exciton-plasmon coupling at the band edges takes place. Formation of these new states can be clearly seen by the simulations ongratings with periods 250 nm, 255 nm and 260 nm (Figure 4.14). When periodicity of the grating is increased further, new state starts to deform (Figure 4.15). The dispersion of the new mode increases significantly occupying larger part of the dispersion surface indicating delocalization. This point needs further study.

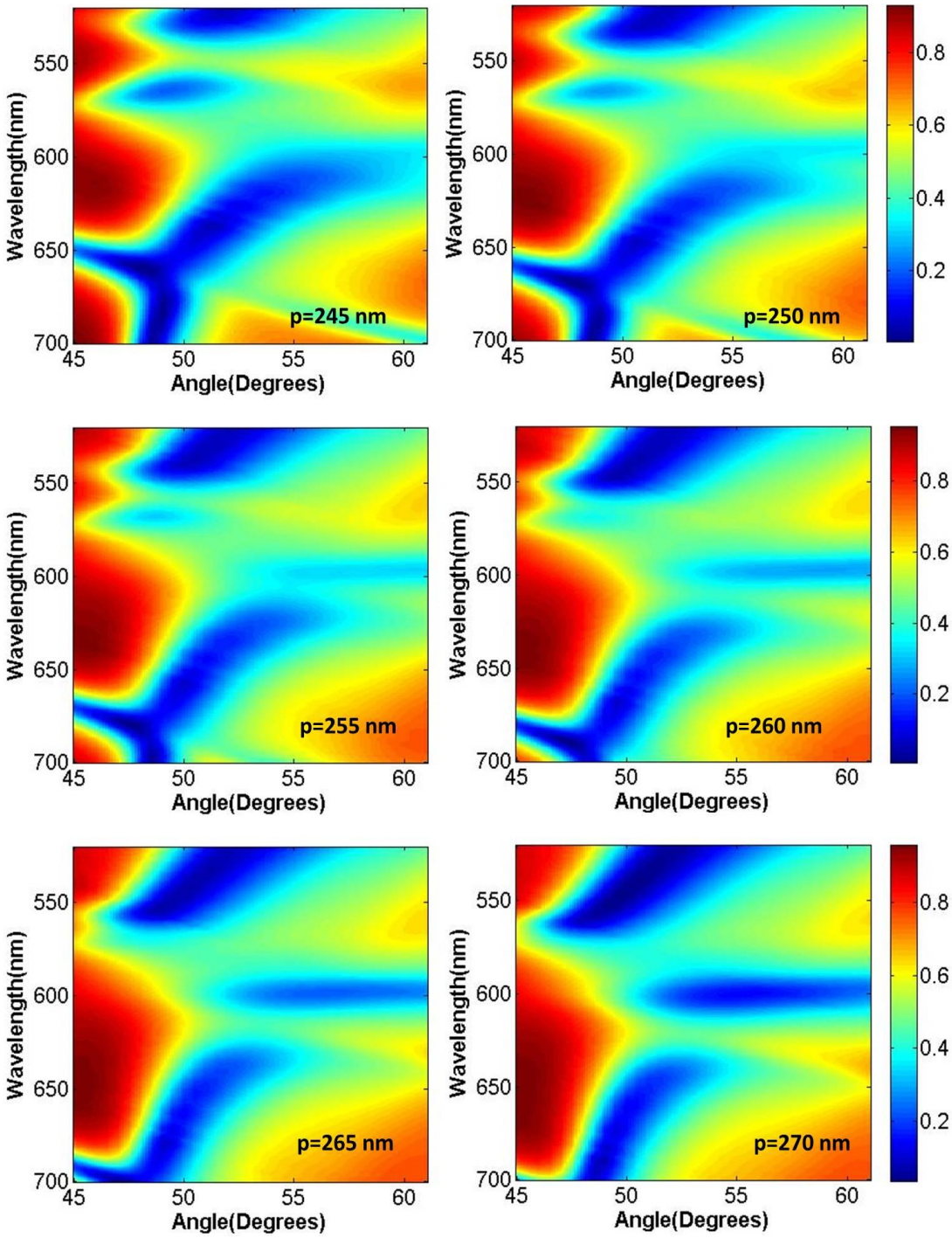

Figure 4.14 Exciton-plasmon coupling as a function of grating periodicity. The periodicity of the uniform grating is changed from 245 nm to 270 nm with a separation of 5 nm.

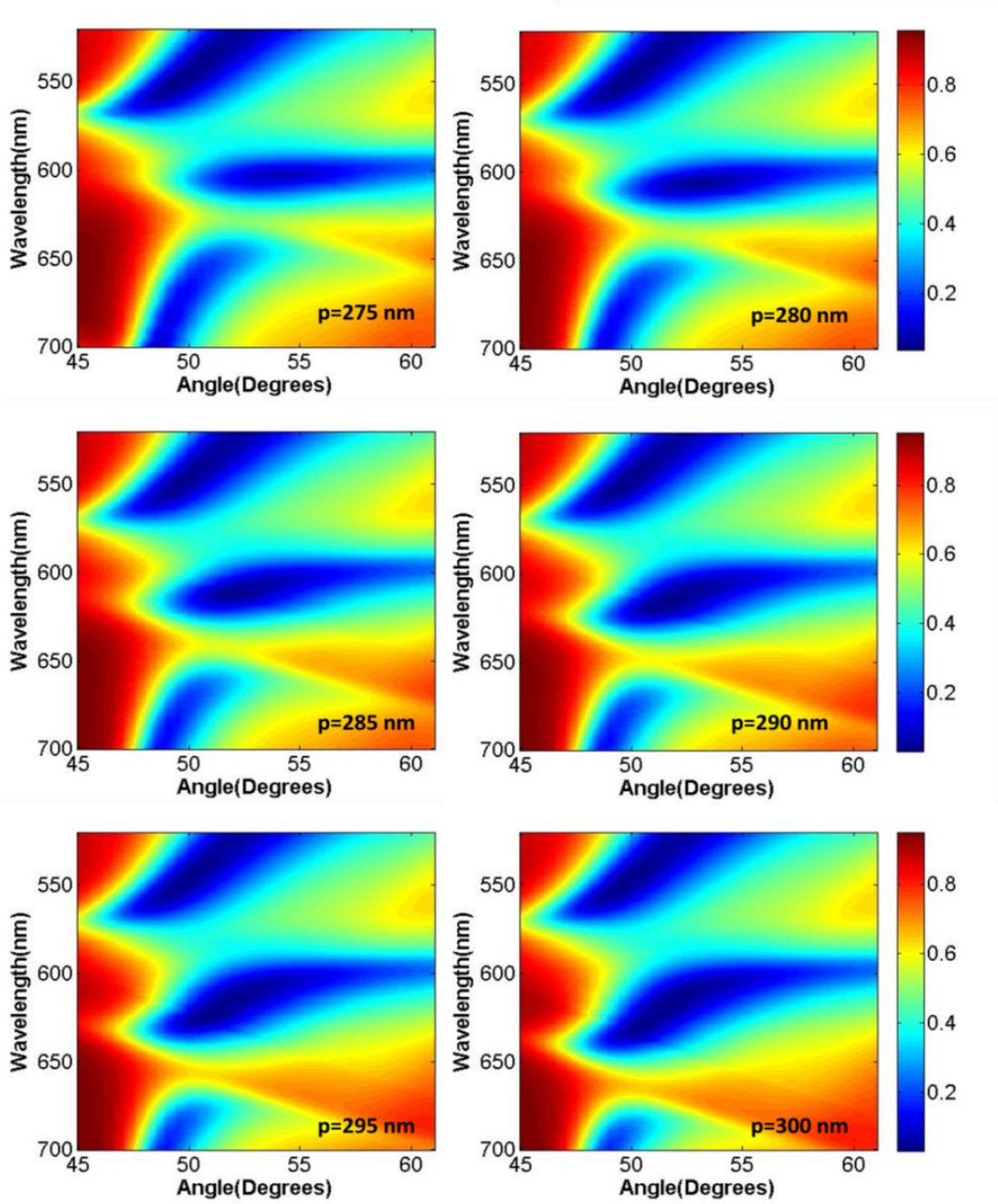

Figure 4.15 Exciton-plasmon coupling as a function of uniform grating periodicity. The periodicity of the uniform grating is changed from 275 nm to 300 nm with a separation of 5 nm.

Effect of grating depth on exciton-plasmon coupling on uniform gratings was also studied. As it has been shown previously, firstly, SPP dispersion is simulated by tuning grating depth of the uniform grating without J-aggregate layer on its surface. When the grating depth is increased, the band gap of the gratings not only shifts to the red but they also get widened (Figure 4.16). When the grating depth is 10 nm the lower polariton branch breaks up with a very narrow opening. The band gap becomes pronounced as the grating depth increases. When the grating depth is 15 nm plasmonic band gap opens up and becomes well established when the grating depth is d=20 nm. The band gap widens as the grating depth increases up to 35 nm.

After the study on bare uniform gratings, effect of grating depth on exciton-plasmon coupling on uniform gratings was also investigated. We observed an unexpected coupling of excitons and plasmons at the tail of band edges on the uniform grating with 255 nm period and 40 nm depth in the Figure 4.14. Therefore, for a fixed periodicity of 255 nm, depth of uniform gratings was altered from 20 nm to 70 nm by in steps of 10 nm and the resulting dispersion curves are shown in Figure 4.17. As can be easily seen in Figure 4.17, a splitting occurs at the wavelength that corresponds to absorption line of J-aggregate for 20 nm grating depth. As the grating depth increases, there occurs splittings at edges of both upper and lower branches clearly seen at grating depth of 30 nm. As we stated indicates of calculations with uniform gratings without J-aggregates calculations, lower branch shifts to longer wavelengths with increase in grating depth. Further increase in the grating depth decreases coupling efficiency and splitting at the upper and lower branches becomes weakened.

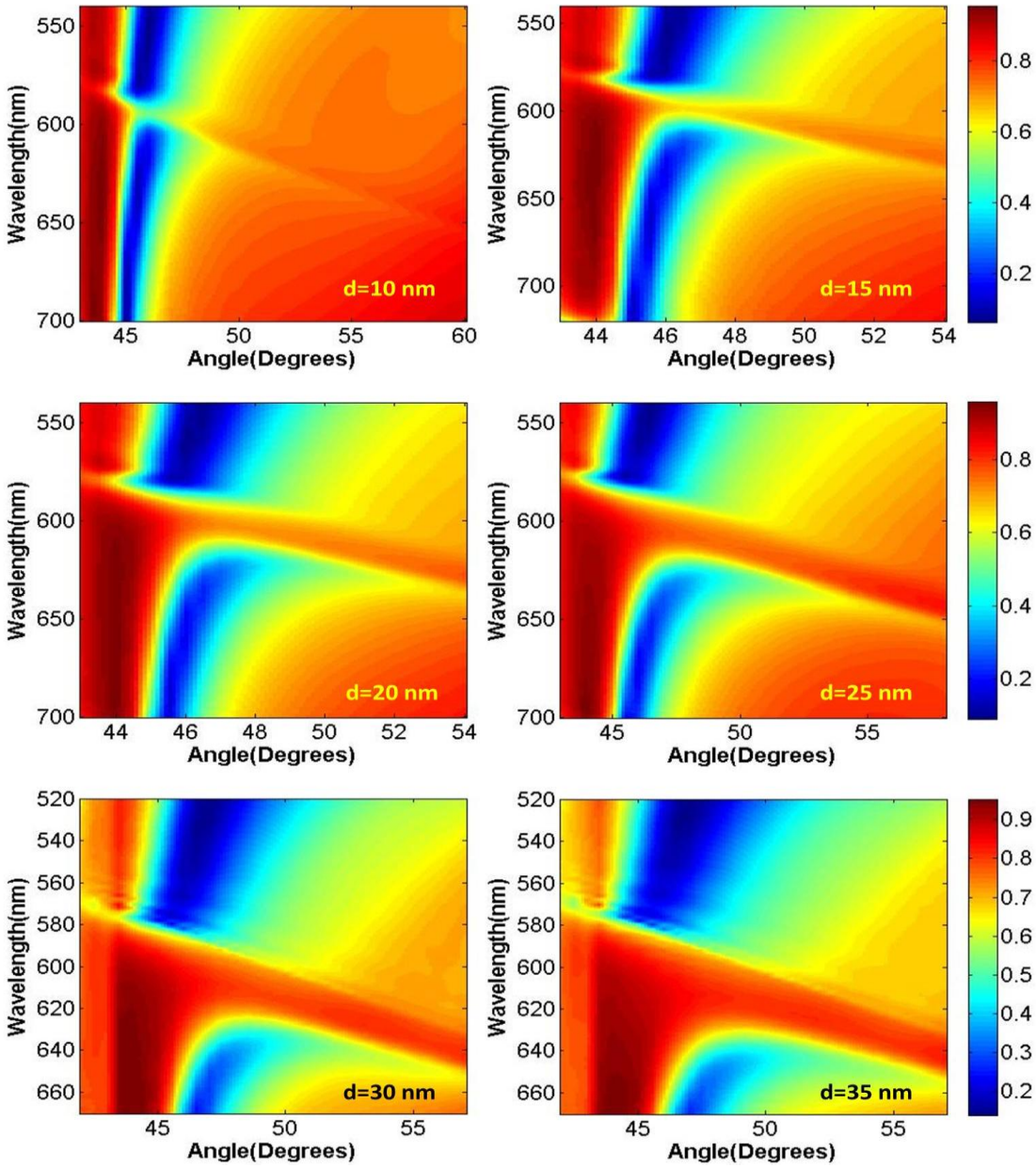

Figure 4.16 SPP reflection curves as a function of uniform grating depth (from 10 nm to 35 nm with a steps of 5 nm)

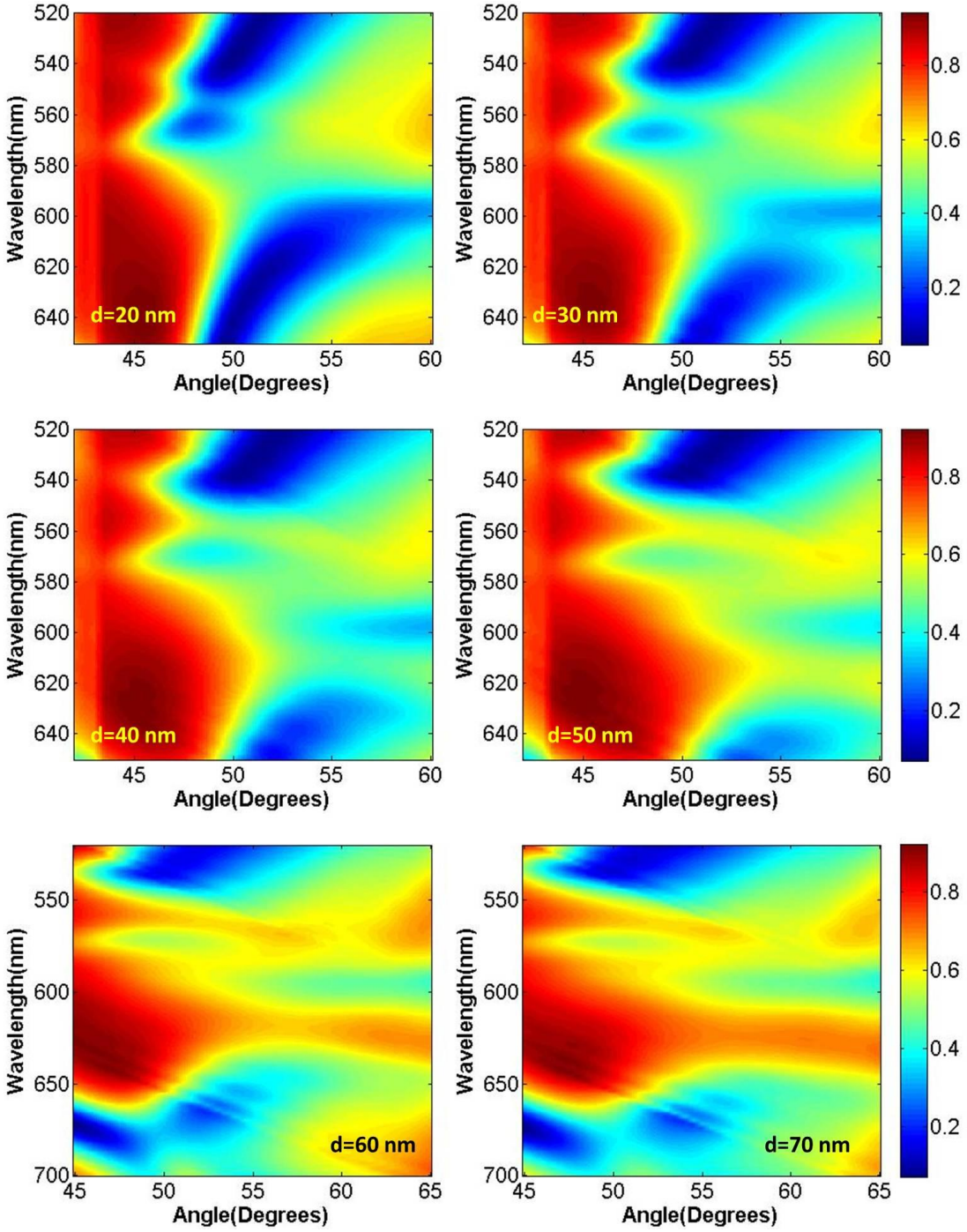

Figure 4.17 Exciton-plasmon coupling as a function of uniform grating depth (from 20 nm to 70 nm with a steps of 10 nm).

4.4 Exciton-plasmon coupling on Moiré surfaces

Exciton-plasmon coupling on flat and uniform grating surfaces has been discussed. Now, exciton-plasmon coupling on Moiré surfaces containing plasmonic cavities will be explored. By using two sinus functions having slightly different periods, simulation surfaces are patterned as Moiré surfaces. Moire surfaces have nodes and antinodes in their spatial distribution with phase shift of π upon crossing the nodes. Ag which is for supporting plasmonic modes and J-Aggregate which is for excitonic layers are placed on a glass substrate, respectively. Light source and reflection monitor were placed on the glass substrate. Bloch boundaries on lateral and several perfectly matching layers (PML) on vertical are the boundary conditions for this simulation.

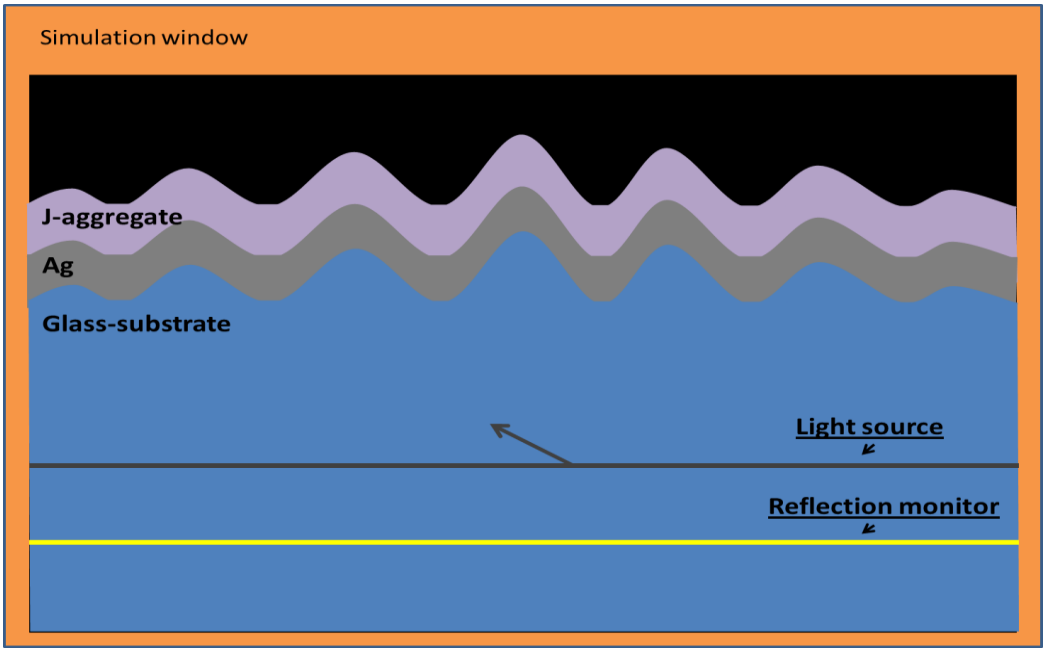

Figure 4.18 Simulation window of exciton-plasmon coupling on Moiré Surface

To generate the Moiré surface structure shown in Figure 4.18, expression shown below is used,

$$\sin\frac{2\pi x}{\lambda_1} + \sin\frac{2\pi x}{\lambda_2} \tag{2.76}$$

where $\boldsymbol{\lambda_1}$ and $\boldsymbol{\lambda_2}$ are slightly different periods of sine functions. Effect of cavity size on exciton-plasmon coupling is investigated in detail in this part of the thesis. As it is demonstrated in Figure 4.19 three states are simulated (a) bare Moiré surface containing cavity size from 2.5 μm to 9.0 μm, (b) with a thin layer of PVA film, which causes red shift of plasmon resonance and (c) with J-aggregate layer, which results in splitting of the cavity mode.

Formation of the cavity and calculation of the cavity size are discussed in details in sec. 2.3.1. We start with the effect of exciton-plasmon coupling in 2.5 μm Moiré surfaces. Due to the periodic nature of the boundary conditions (Bloch) we are in fact dealing with multiple cavities. When the cavity size is small, the possibility of plasmon modes hopping from one cavity to the other remains [26].

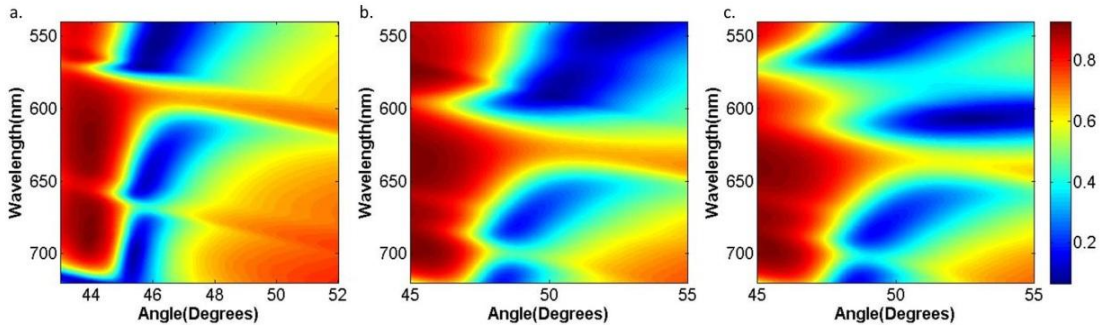

Figure 4.19 Exciton-plasmon coupling on a Moiré Surface with a period of 2.5 μm. (a) bare Moiré surface, (b) PVA coated Moiré surface, (c) J-aggregate coated Moiré surface

For a Moiré surface with cavity size of 2.5 μm, it is clearly seen that cavity mode first shifts to the longer wavelengths and then splits into two modes, which is indicative ofexciton-plasmon coupling, Figure 4.19. Red shift is expected because of increased effective index due to PVA overlayer. Splitting is at the wavelength which correspond to absorption, 590 nm. We note that the two states observing the band gap do not both have dispersion. While the state with higher energy seems to be dipersionless the lower energy state has pronounced dispersion. This suggests that they are not the same in nature.

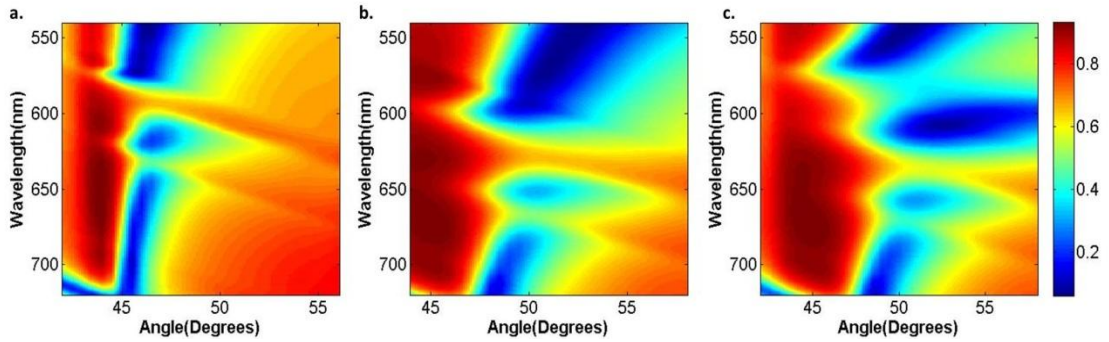

Figure 4.20 Exciton-plasmon coupling on Moiré Surface with a period of 5μm.

In Figure 4.20 simulation results for Moiré surface with cavity size of 5μm. The effect of air, pure PVA and J-Aggregate on polaritonic modes was studied. As the cavity size widens, coupling between adjacent cavities modes decreases.

To match the absorption line in the middle of the cavity state, periods of Moiré surface are tuned. However, the larger the cavity size becomes, the more localized cavity state is. So it becomes harder to match the cavity mode with the absorption line. As a result Rabi splitting in the cavity mode is barely seen in 9μm cavity size case (Figure 4.21c)

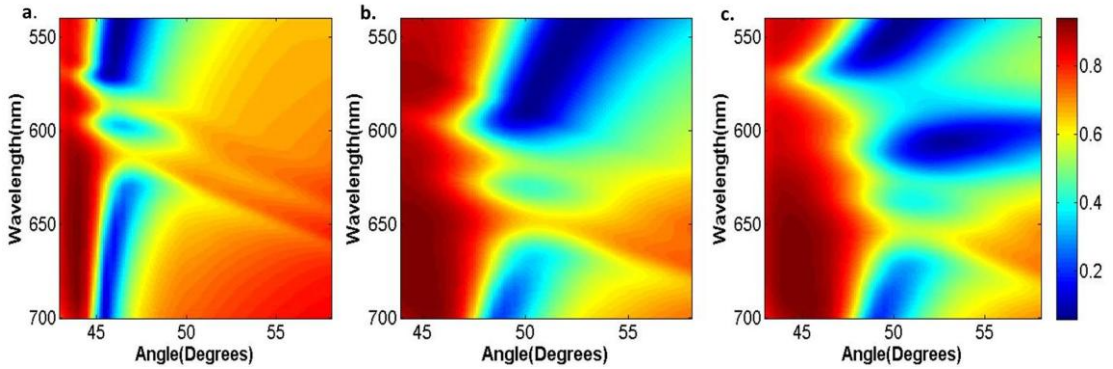

Figure 4.21 Plasmon Exciton coupling on Moiré Surface with a period of 9μm

Three states are simulated a) Moiré surface with 9μm cavity size only, b) with PVA which causes red shift due to changing effective index, and c) with J-aggregate which resulted with Rabi splitting of cavity mode.

For 2.5 μm, 5μm and 9.0 cavity size Moiré surfaces, exciton-plasmon coupling which results with Rabi splitting of cavity state is shown.

Chapter 5

Results

In this part of the thesis, the results obtained from FDTD simulations and polarization dependent spectroscopic reflection measurements will be discussed and conclusions drawn will be summarized. Exciton-plasmon coupling was studied on flat, uniform grating, and Moiré surfaces. Aggregated TDBC molecules (J-aggregate) were used as a exciton matter component and metal coated surfaces were used to support propagation of surface plasmons. TDBC molecules embedded in PVA matrix were placed on metal coated surfaces. Exciton-plasmon coupling was tuned by varying the optical density of the TDBC molecules in PVA matrix and varying the thickness of the metal film. FDTD simulations were performed in order to understand plasmon and exciton interaction in these multilayer structures.

Before studying exciton-plasmon coupling on J-aggregate coated plasmonic surfaces, dispersion of surface plasmon polaritons on flat, uniform and Moiré surfaces were studied in the Kretschmann configuration. The simulation results are in excellent agreement with the previously demonstrated experimental observations [26]. Firstly, on flat metal surfaces, effects of Lorentz oscillator strength were modeled. For a constant metal film thickness and a constant J-aggregate film thickness, Lorentz oscillator strength was varied and dispersion curves were obtained. Rabi splitting energies were calculated from the dispersion curves as stated by Bellessa et al [17].

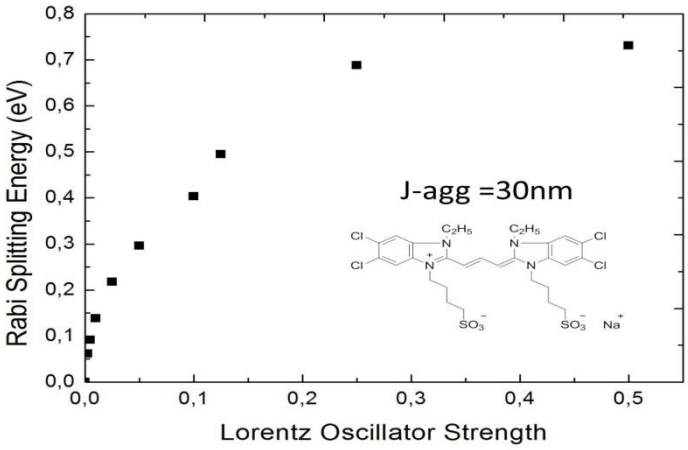

Figure 5.1 Rabi Splitting energy vs. Lorentz oscillator strength. As the Lorentz total oscillator strength increases the Rabi splitting energy increases. Rabi splitting as large as 700 meV seem to be possible.

As it is clearly seen in Figure 5.1 Rabi splitting energy increases with an increase in Lorentz oscillator strength. The inset indicates the chemical structure of a TDBC molecule.

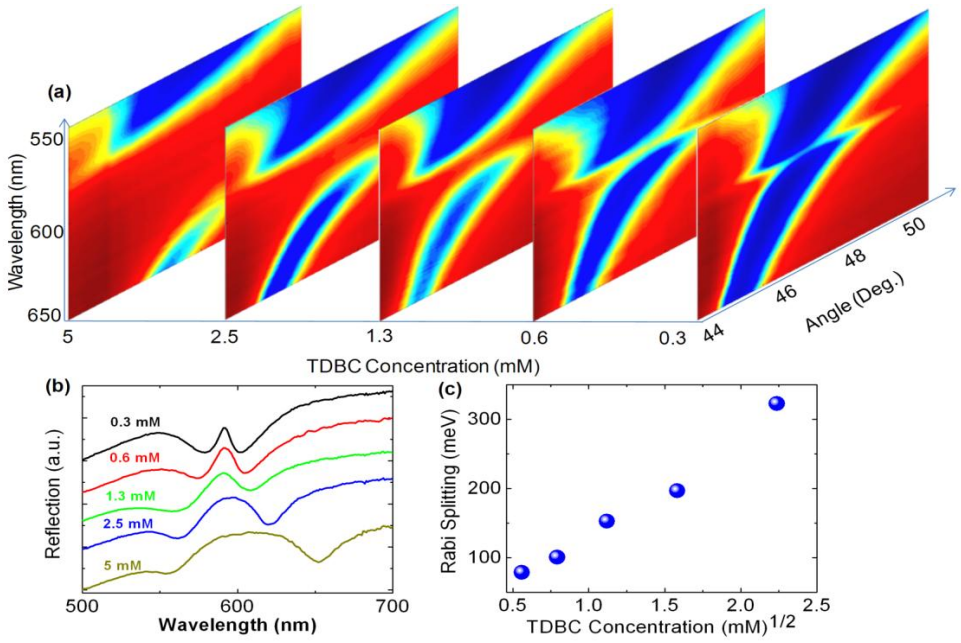

Figure 5.2 Plasmon-exciton coupling as a function of TDBC concentration. (a) Evolution of polariton reflection curves with varying concentration of TDBC molecules in the PVA matrix. As the concentration of the TDBC molecules increases

in the PVA matrix, plasmon-exciton coupling energy or Rabi splitting energy increases. (b) Polariton reflection curves of thin Ag films containing active layer of varying concentration of TDBC molecules in the PVA matrix. (c) Rabi splitting increases linearly with the square root of the TDBC concentration in the PVA matrix [35].

When the dye concentration of the TDBC molecules within the PVA matrix is increased, first a gap occurs and then it gets widened in Figure 5.2a. Rabi splitting energy is directly proportional to the square root of the TDBC concentration in the PVA matrix. It is worth mentioning here that the TDBC dye concentration in the PVA matrix corresponds to the Lorentz oscillator strength in the simulations.

Further experiments were conducted to study effects of metal film thickness on exciton-plasmon coupling. Lorentz oscillator strength was fixed to be 0.1 and silver film thickness is varied from 20 nm to 50 nm. By fixing Lorentz total oscillator strength, optical density of TDBC molecules was fixed in the PVA matrix and hence exciton- plasmon coupling energy was constant. Dispersion curves were taken in the Kretschmann configuration. Rabi splitting energy was calculated in the same way as before.

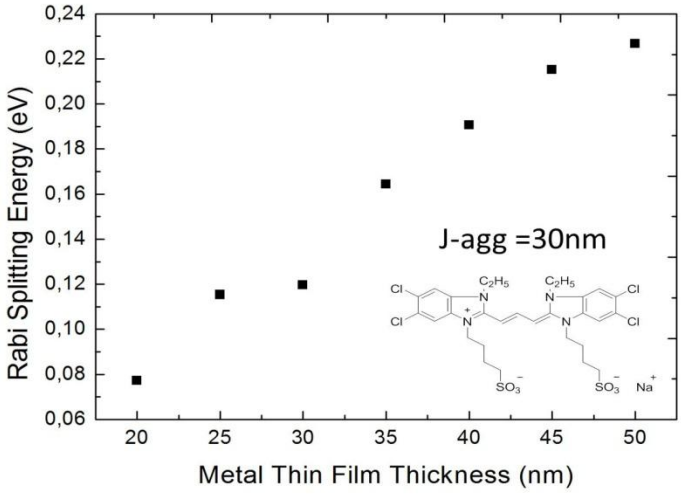

Figure 5.3 The concentration of TDBC molecules were kept constant while the thickness of the plasmonic layer was varied from 20 nm to 50 nm. The Rabi splitting energy increases with an increase in TDBC concentration.

As show in Figure 5.3, Rabi splitting is also function of thickness. This simulation results are also confirmed with experimentally.

In simulations of uniform grating, there is not expecting any coupling. For fixed grating depth period of the uniform grating was altered. Although there is not any plasmonic states in the band gap, when absorption line (at 590 nm) intercept with the band gap, a weak coupling is observed due to the exciton-plasmon coupling at the band edges. Formation of weak coupling can be clearly seen by difference between the periods 250 nm, 255 nm and 260 nm in Figure 5.4

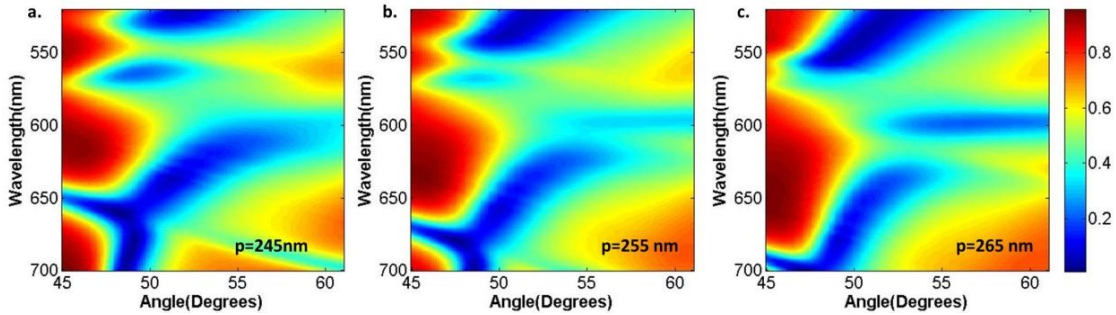

Figure 5.4 Dispersion curves for uniform gratings (p=245 nm, 255 nm, 265 nm)

By setting period of uniform grating at 285 nm, effect of grating depth on exciton-plasmon coupling was also studied. While grating depth (d) increasing, band gap of the gratings are not only shifts to the red but also get widened.

Final simulations were on Moiré surfaces as a function of cavity size. 2.5 μm, 5μm 9μm and 15 μm cavity size Moiré surfaces with fixed strength, metal thickness were simulated and dispersion curves were plotted. Rabi splitting was calculated as before and Q factors were calculated from dispersion curves.

Q factor increases with the increase in cavity size while Rabi splitting energy decreases with Q factor, Figure 5.5. Increase in the Q factor is the result of confinement of cavity state as it size growing.

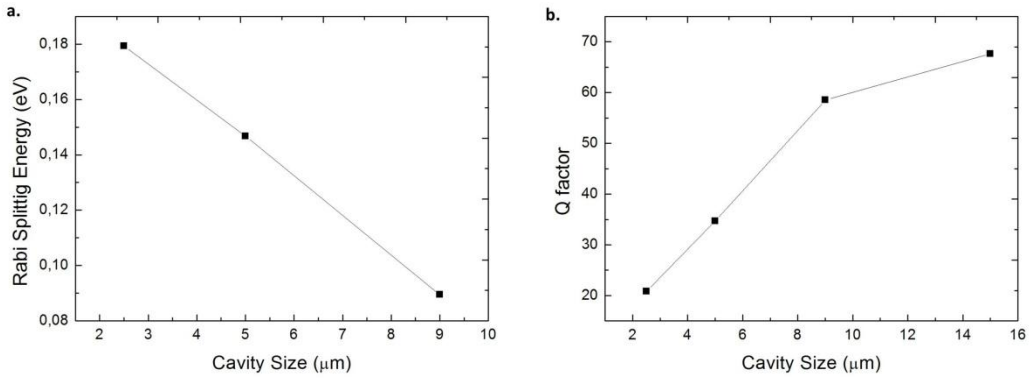

Figure 5.5 Rabi splitting and Q factor response of Moiré surfaces as a function of cavity size**.**

It should be noted here that the calculated Rabi splitting values from the wavelength versus angle polariton dispersion curves should be different from the energy versus wave vector polariton dispersion curves. Since the wavevector $k = \frac{2\pi}{\lambda}\sin(\theta)$is not constant for a fixed incidence angle for the lower and upper polaritonic branches. However, we calculated the Rabi splitting only from wavelength versus angle polariton dispersion curves since during this study we monitored relative change of the Rabi splitting energy as a function of different parameters.

In summary, the following results have been obtained during the course of this thesis studies.

Exciton-plasmon coupling on several metallic surfaces with flat and corrugated surfaces was experimentally and theoretically studied in detail. The effect of various parameters such as periodicity, grating depth, Lorentz oscillator strength, metal thin film thickness and cavity size on exciton-plasmon was studied in detail. Rabi splitting and a cavity state were observed in several cases.

Rabi splitting energy was found to increase with the square root of TDBC concentration. That is the separation between the lower and upper polariton branches can be defined as a function of concentration.

Exciton-plasmon coupling can be tuned by varying the plasmonic layer thickness.

For future studies, the nature of the faint new state that occurs due to exciton-plasmon interaction on flat metal surfaces needs to be investigated further. Dispersion of this new state as well as its polarization dependence needs to be investigated in more detail (see Figure 4.10 in sec. 4.2) to decide it is whether purely an excitonic state or a state related to the coupling of excitons with plasmons.

Tuning exciton-plasmon coupling over metal thin film thickness, dye concentration, grating depth and periocity, and cavity size give us ability to control the dispersion diagram. This control makes it possible to fabricate efficient and convenient cavities for enhanced Raman spectroscopy and nonlinear plasmonic applications leading to demonstration of plasmonic lasers.

Bibliography

[1] R. H. Ritchie, "Plasma Losses by Fast Electrons in Thin Films," *Phys. Rev.*, p. 874, 1957.

[2] H. A. Atwater, "The promise of plasmonics," *Sci. Am.*, vol. 296, pp. 56-63, 2007.

[3] C. Symonds, C. Bonnand, J. C. Plenet, A. Bréhier, R. Parashkov, J. S. Lauret, E. Deleporte and J. Bellessa, "Particularities of surface plasmon–exciton strong coupling with large Rabi splitting," *New Journal of Physics,* vol. 10, p. 065017(11), 2008.

[4] M. W. Maqsood, R. Mehfuz and K. J. Chau, "High-throughput diffraction-assisted surface-plasmon-polariton coupling by a super-wavelength slit," *Optical Society of America*, vol. 18, no. 21, pp. 21669-21677, 2010.

[5] S. A. Maier and H. A. Atwater, "Plasmonics: Localization and guiding of electromagnetic energy in metal/dielectric structures," *Jurnal of Applied Physics*, vol. 98, pp. 011101 (1)-(10), 2005.

[6] J. R. Krenn and J. C. Weeber, "Surface plasmon polaritons in metal stripes and wires," *Phil. Trans. R. Soc. Lond. A*, vol. 362, p. 739–756, 2004.

[7] J. M. Pitarke, V. M. Silkin, E. V. Chulkov and P. M. Echenique, "Theory of surface plasmons and surface plasmon polaritons," *Reports on Progress in Physics*, pp. 1-87, 2007.

[8] A. V. Zayats, I. I. Smolyaninov and A. A. Maradudin, "Nano-optics of Surface Plasmon Polaritons," *Physic Reports*, no. 405, pp. 131-314, 2005.

[9] J. A. Schuller, E. S. Barnard, W. Cai, Y. C. Jun, J. S. White and M. L. Brongersma, "Plasmonics for extreme light concentration and manipulation," *Nature Materials*, vol. 9, pp. 193-204, 2010.

[10] S. S. Senlik, A. Kocabas and A. Aydinli, "Grating based band gap cavities," *Optics Express*, vol. 17, no. 18, pp. 15541-15549, 2009.

[11] C. Weisbuch, M. Nishioka, A. Ishikawa and Y. Arakawa, *New Journal of Physics*, vol. 10, pp. 065017 (1)-(11), 1992.

[12] M. A. Noginov, G. Zhu, M. Mayy, B. A. Ritzo, N. Noginova and V. A. Podolskiy, "Stimulated emision of surface plasmon polaritons," *Physical Review Letters,* vol. 101, no. 22, pp. 226806-1,4, 2008.

[13] I. Pockrand, A. Brillante and D. Möbius, "Exciton-surface plasmon coupling: An experimental investigation," *J. Chem. Phys.,* vol. 77, no. 12, pp. 6289-6295, 1982.

[14] A. Trügler and U. Hohenester, "Strong coupling between a metallic nanoparticle and a single molecule," *Physical Review B ,* vol. 77, pp. 115403-1,6, 2008.

[15] D. G. Lidzey, D. C. Bradley, A. Armitage, S. Walker and M. S. Skolnick, "Photon metal hybridization of Frenkel excitons in organic semiconductor mickrocavities," *Science,* vol. 288, no. 1620, 2000.

[16] T. Yoshie , A. Scherer , J. Hendricson, G. Khitrova, H. Gibbs, G. Rupper, C. Ell, O. Shchekin and D. Deppe, "Vacuum Rabi Splitting with a single quantum dot in a photonic crystal nanocavity," *Nature,* no. 432, p. 200, 2004.

[17] J. Bellessa , C. Symonds, K. Vynck, L. Beaur , A. Brioude and A. Lemaitre , "Giant Rabi splitting in metal/semiconductor nanohybrids," *Superlattices and Microstructures,* vol. 49, pp. 209-216, 2011.

[18] G. Boidse and A. Harmer, Chemical and Biochemical Sensing with Optical Fibers and Waveguides, Boston: Arthech House, 1996.

[19] S. M. Nie and S. R. Emery, *Science,* no. 275, p. 1102, 1992.

[20] R. F. Oulton, V. J. Sorger, T. Zentgraf, R. M. Ma, C. Gladden, L. Dai, G. Bartal and X. Zhang, "Plasmon lasers at deep subwavelength scale.," *Nature,* vol. 461, no. 7264, pp. 629-632, 2009.

[21] J. D. Jackson, Classical Electrodynamics, John Wiley & Sons, Inc., 1998.

[22] N. W. Ashcroft and N. D. Mermin, Solid State Physics, Harcourt, Inc, 1976.

[23] S. A. Maier, Plasmonics, Berlin: Springer, 2007.

[24] A. D. McFarland, M. A. Young, J. A. Dieringer and R. P. Van Duyne, "Wavelength-scanned surface-enhanced Raman excitation spectroscopy," *J. Phys. Chem.,* vol. B 109, no. 22, pp. 11279-11285, 2005.

[25] S. Balci, A. Kocabas, C. Kocabas and A. Aydinli, "Localization of surface plasmon polaritons in hexagonal arrays of Moiré cavities," *Applied Physics Letters,* vol. 98, pp. 031101-1,031101-3, 2011.

[26] S. Balci, M. Karabiyik, A. Kocabas, C. Kocabas and A. Aydinli, "Coupled plasmonic cavities on Moire surfaces," *Plasmonics,* pp. 429-436, August 2010.

[27] J. R. Tischler, M. S. Bradley, Q. Zhang, T. Atay, A. Nurmikko and V. Bulovic, "Solid state cavity QED: Strong coupling in organic thin films.," *Organic Electronics 8,* no. 94-113, 2007.

[28] C. C. Gerry and P. L. Knight, Introductory Quantum Optics, Cambridge: Cambridge University Press, 2005.

[29] J. B. Schneider, Understanding the Finite-Difference Time-Domain, 2011, pp. 34-39.

[30] E. D. Palik, Handbook of optical constants of solids, Boston: Academic Press, 1985.

[31] D. E. Gomez, K. C. Vernon, P. Mulvaney and T. J. Davis, "Surface Plasmon Mediated Strong Exciton-Photon Coupling in Semiconductor Nanocrystals," *Nono Letters 10,* pp. 274-278, 2010.

[32] Y. Zhu, D. J. Gauthier, S. Morin, Q. Wu, H. J. Carmichael ve T. W. Mossberg, *Phys. Rev. Lett.,* cilt 64, p. 2499, 1990.

[33] S. Balci, C. Kocabas, S. Ates, E. Karademir, O. Salihoğlu and A. Aydinli, "Tuning Surface Plasmon-Exciton Coupling," *(Submitted),* 2012.

[34] A. Kocabas, S. S. Senlik and A. Aydinli, "Slowing down surface plasmons on a Moiré surface," *Physical Review Letters,* vol. 102, pp. 063901(1)-(4), 2009.